ARTICLE   OPEN

Check for updates

Tailoring magnetic hysteresis of additive manufactured Fe-Ni permalloy via multiphysics-multiscale simulations of process-property relationships

Yangyiwei Yang [1]✉, Timileyin David Oyedeji[1], Xiandong Zhou[2], Karsten Albe [3] and Bai-Xiang Xu [1]✉

Designing the microstructure of Fe-Ni permalloy produced by additive manufacturing (AM) opens new avenues to tailor its magnetic properties. Yet, AM-produced parts suffer from spatially inhomogeneous thermal-mechanical and magnetic responses, which are less investigated in terms of process modeling and simulations. We present a powder-resolved multiphysics-multiscale simulation scheme for describing magnetic hysteresis in AM-produced material, explicitly considering the coupled thermal-structural evolution with associated thermo-elasto-plastic behaviors and chemical order-disorder transitions. The residual stress is identified as the key thread in connecting the physical processes and phenomena across scales. By employing this scheme, we investigate the dependence of the fusion zone size, the residual stress and plastic strain, and the magnetic hysteresis of AM-produced $Fe_{21.5}Ni_{78.5}$ on beam power and scan speed. Simulation results also suggest a phenomenological relation between magnetic coercivity and average residual stress, which can guide the magnetic hysteresis design of soft magnetic materials by choosing appropriate processing parameters.

INTRODUCTION

The Fe-Ni permalloy has been widely studied in recent decades owing to its extraordinary magnetic permeability, low coercivity, high saturation magnetization, mechanical strength, and magneto-electric characteristics. This material has been widely employed in conventional electromagnetic devices, such as sensors and actuators, transformers, electrical motors, and magnetoelectric inductive elements. Fe-Ni-based permalloys modified with additives are also promising candidate materials for multiple novel applications, such as wind turbines, all-electric vehicles, rapid powder-conversion electronics, electrocatalysts, and magnetic refrigeration[1–4].

Due to the increasing importance of additive manufacturing (AM) technologies, the possibilities of designing soft magnetic materials by AM have been explored in a number of studies[5–12]. However, due to the delicate interplay of process conditions and resulting properties, there are several open questions that need to be answered in order to obtain AM-produced Fe-Ni permalloy parts with the desired property profile. Magnetic properties of the Fe-Ni system depend on the chemical composition, as depicted in Fig. 1a. $Fe_{21.5}Ni_{78.5}$ is typically selected targeting the chemical-ordered low-temperature FCC phase (also known as awaruite, $L1_2$, or γ' phase, as the phase-diagram shown in Supplementary Fig. 1a), which possesses a minimized coercivity and peaked magnetic permeability[8,13]. The main problem is to increase the generation of γ' phase using AM, as the phase transition kinetics from the chemical-disordered high-temperature FCC phase (also known as austenite, A1, or γ phase) to the chemical-ordered γ' phase is extremely restricted[14]. On the laboratory timescale, growing the γ' phase into considerable size requires annealing times on the order of days[15–19]. Due to the rapid heating and cooling periods, only the γ phase exists in AM-processed parts[9].

Combining in-situ alloying with AM methods allows to stabilize the γ' phase in printed parts[8,20], but the restricted kinetics still limit the growth of a long-range ordered phase[14]. Another question concerns the influences of associated phenomena on magnetic hysteresis. Although there are studies on the effects of crystallographic texture[11,21], a pivotal discussion regarding interactions among residual stress, microstructures, and physical processes leading to the magnetic hysteresis behavior is unfortunately missing.

Recently, it has been shown that soft magnetic properties can be designed by controlling magneto-elastic coupling[22–24]. Along these lines, the residual stress caused by AM and the underlying phase transitions could be key for tuning the coercivity in an AM-processed Fe-Ni permalloy. Micromagnetic simulations by Balakrishna et al.[23] presented that magneto-elastic coupling plays an important role in governing magnetic hysteresis, as the existence of the pre-stress shifts the minimized coercivity from the composition $Fe_{25}Ni_{75}$ to $Fe_{21.5}Ni_{78.5}$, while the magneto-crystalline anisotropy is zero at $Fe_{25}Ni_{75}$ but non-zero at $Fe_{21.5}Ni_{78.5}$. Based on a vast number of calculations, the dimensionless constant $(C_{11} - C_{12})\lambda_{100}^2/2K_u \approx 81$ was proposed as a condition for low coercivity along the $\langle 100 \rangle$ crystalline direction for cubic materials (incl. Fe-Ni permalloy)[24]. Here, C_{11} and C_{12} are the components of the stiffness tensor, λ_{100} is the magnetostrictive constant, and K_u is the magneto-crystalline constant. Nevertheless, the influence of the magnitude and the states of the residual stress were not comprehensively analyzed. Yi et al. discussed magneto-elastic coupling in the context of AM-processed Fe-Ni permalloy[22]. The simulations were performed with positive, zero, and negative magnetostrictive constants under varying beam power. The results showed that the coercivity of the Fe-Ni permalloy with both positive and negative magnetostrictive

[1]Mechanics of Functional Materials Division, Institute of Materials Science, Technische Universität Darmstadt, Darmstadt 64287, Germany. [2]Failure Mechanics and Engineering Disaster Prevention Key Laboratory of Sichuan Province, College of Architecture and Environment, Sichuan University, Chengdu 610207, China. [3]Materials Modelling Division, Institute of Materials Science, Technische Universität Darmstadt, Darmstadt 64287, Germany. ✉email: yangyiwei.yang@mfm.tu-darmstadt.de; xu@mfm.tu-darmstadt.de
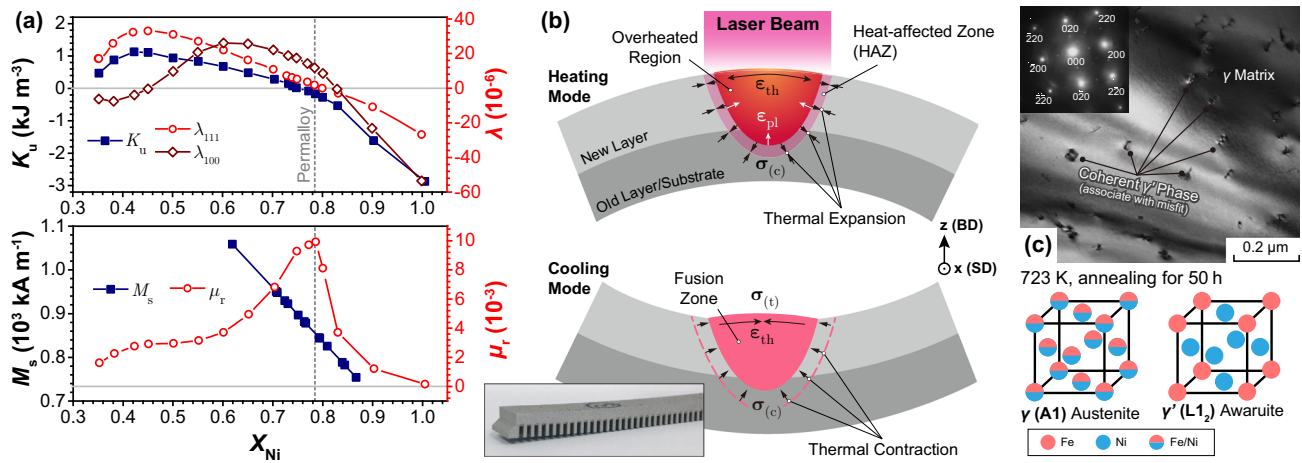
Fig. 1 Emerging issues during additive manufacturing of Fe-Ni permalloy. a Ni concentration dependent magnetic properties, incl. magneto-crystalline anisotropic constant K_u, magnetostriction constants λ_{100} and λ_{111}, saturation magnetization M_s and initial relative permeability μ_r, modified with permission from Balakrishna et al.[23]. **b** Schematics of temperature gradient mechanism (TGM) for explaining the generation of residual stress in heating and cooling modes, where the tensile ($\sigma_{(t)}$) and compressive ($\sigma_{(c)}$) stress states, and strains due to thermal expansion (ε_{th}) and activated plasticity (ε_{pl}) are denoted. Inset: A bent AM-processed part due to residual stress. Image is reprinted with permission from Takezawa et al.[27] under the terms of the Creative Commons CC-BY 4.0 license. **c** Bright-field image of a Fe-Ni permalloy microstructure after annealing at 723 K for 50 h. Inset: electron diffraction pattern of the microstructure. SEM and electron diffraction images are reprinted with permission from Ustinovshikov et al.[19].

constants rises with increasing beam power. In contrast, the permalloy with zero magnetostrictive constant showed no dependence on the beam power. This demonstrates the necessity of magneto-elastic coupling in tuning coercivity in AM-produced permalloy and illustrates the potential of tailoring magnetic hysteresis of permalloys via controlling the residual stress during AM.

Understanding the residual stress in AM and its interactions with other physical processes, such as thermal and mass transfer, grain coarsening and coalescence, and phase transition, is never the oak that felled at one stroke. Taking the popular selective laser melting/sintering (SLM/SLS) method as an instance, the temperature gradient mechanism (TGM) explains the generation of residual stress by considering the heating mode and the cooling mode[25–27]. The heating mode presents a counter-bending with respect to the building direction (BD) of newly fused layers (Fig. 1b). This is because the thermal expansion in an upper overheated region gets restricted by the lower old layer/substrate. Plastic strain can also be generated due to the activated plasticity of the material and compensate the local stress around the heat-affected zone. The cooling mode, in contrast, presents a bending towards the BD of the newly fused layer due to the thermal contraction between the fusion zone and the old layer/substrate.

It should be noted that TGM only provides a phenomenological aspect by employing the idealized homogeneous layers. In the practical SLM/SLS, varying morphology and porosity of the powder bed create inhomogeneity in not only the temperature field but also the on-site thermal history on the mesoscale (10–100 μm), inciting varying degrees of thermal expansion, and eventually leading to the development of the thermal stress in various degree. Stochastic inter-particle voids and lack-of-fusion pores also create evolving inhomogeneity in material properties on the mesoscale[28,29], leading to the shifted local stress conditions interpreted by TGM. In other words, mesoscopic inhomogeneity and coupled thermo-structural evolution should act as long-range factors in residual stress development. On the other hand, due to the relatively smaller lattice parameter, the continuous growth of the γ' phase would also result in the increasing misfit stress between itself and the chemical-disordered γ matrix[18,19] (as also presented in Fig. 1c). Therefore, the nanoscopic solid-state phase transition also contributes to the development of residual stress as

a short-range fluctuation, which is almost effectless to the mesoscopic phenomena yet still influences the local magnetic behavior[23]. To sum up, the residual stress from AM processes that eventually affects the magnetization reversal via magneto-elastic coupling should already reflect such long-range (morphology and morphology-induced chronological-spatial thermal inhomogeneity) and short-range factors (misfit-induced fluctuation). This is the central challenge that this work addresses.

In this work, we developed a powder-resolved multiphysics-multiscale simulation scheme to investigate the hysteresis tailoring of Fe-Ni permalloy by AM under a scenario close to practical experiments. This means that the underlying physical processes, including the coupled thermal-structural evolution, chemical order-disorder transitions, and associated thermo-elasto-plastic behaviors, are explicitly considered and bridged by accounting for their chronological-spatial differences. The influences of processing parameters (notably the beam power and scan speed) are analyzed and discussed on distinctive aspects, including the size of the fusion zone, the development of residual stress and accumulated plastic strain, the γ/γ' transition under the residual stress, and the resulting magnetic coercivity of manufactured parts. It is anticipated that the presented work could provide transferable insights in selecting processing parameters and optimizing routine for producing permalloy using AM, and deliver a comprehensive understanding of tailoring the hysteresis of soft magnetic materials in unconventional processing.

RESULTS

Multiphysics-multiscale simulation scheme

In this work, we consider SLS as the AM approach due to its relatively low energy input as compared to other methods, like SLM. SLS allows us to obtain a stable fusion zone and thus to gain better control of the residual stress development since we don't need to consider melting and evaporating processes and the associated effects, such as the keyholing and Marangoni convection. The microstructure of SLS-processed parts is porous, which allows us to explore the effects of lack-of-fusion pores on the development of residual stress and plastic strain. Based on an overall consideration of all possible phenomena involved in the
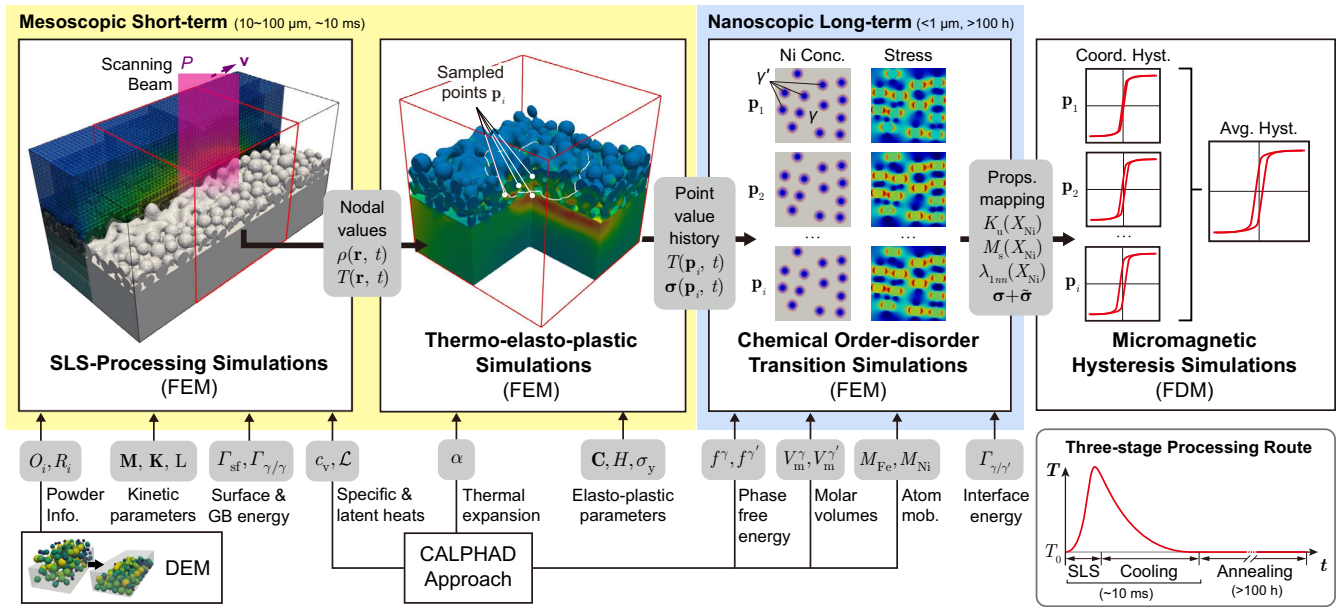
Fig. 2 Multiphysics-multiscale simulations scheme proposed in this work. The workflow and data interaction among methods are illustrated schematically. All the involved quantities are explicitly introduced in the *Method* section. Notice here λ_{1nn} represents λ_{100} and λ_{111}.

SLS of the Fe-Ni permalloy, two chronological-spatial scales are integrated in this work:

(i) On the mesoscale, with the characteristic length of several 100 μm, powders are fused/sintered around the laser spot, creating the fusion zone. Featured phenomena such as partial/full melting, necking, and shrinkage among powders can be observed. High gradients in the temperature field are also expected due to laser scanning and rapid cooling of the post-fusion region. By choosing a typical scan speed of 100 mm s^{-1}, this stage lasts only 10 ms.

(ii) On the nanoscale with a characteristic length well below 1 μm, the chemical order-disorder (γ/γ') transition can be observed once the on-site temperature is below the transition temperature, as presented in Fig. 1c. Owing to the difference in thermodynamic stability, redistribution of the chemical constituents by inter-diffusion between γ and γ' phases is coupled to the phase transition. Due to the extremely restricted kinetics, it would cost several hundred hours of annealing to have the γ' phase formation in a mesoscopic size[15,18,30].

We explicitly consider a three-stage processing route consisting of an SLS, a cooling, and an annealing stage. As shown in the inset of Fig. 2, the domain temperature will rise from a pre-heating temperature (T_0) during the SLS stage. After that, the whole powder bed would gradually cool down to T_0. Finally, the processed powder bed enters the annealing stage at T_0 where the γ/γ' transition continues. No magnetic field is applied during the processing route to eliminate the potential influences from magnetic domain evolution through magnetostriction. The cooling stage lasts three times longer than the SLS stage, and the sequential annealing stage takes far longer than the two other stages. Taking a 500 μm scan section with a typical scan speed of 100 mm s^{-1} as an example, the SLS and cooling stages would last 5 and 20 ms, respectively, and the annealing time is on the order of 100 h. Remarkably, the inhomogeneous and time-varying temperature field in the mesoscopic powder bed can be treated as uniform and nearly constant for the nanoscopic γ/γ' transition, as the heating and cooling stages induced by laser scan are negligible compared to the time required for the γ/γ' transition. Similarly, the mechanical response (notably the residual stress) on

the mesoscopic is also regarded as uniform with respect to sufficiently small nanoscopic domains where the γ/γ' transition occurs. Nonetheless, their long-term effects remain after the first two stages and would further influence the nanoscopic phase formation during the annealing stage, influencing the resultant magnetic hysteresis behavior by electro-magnetic coupling[22,23,31].

The simulations are arranged in a subsequent scheme to recapitulate the aforementioned characteristics on different scales while balancing the computational cost-efficiency, as shown in Fig. 2. Accepting that heat transfer is only strongly coupled with microstructure evolution (driven by diffusion and underlying grain growth) but weakly coupled with mechanical response during the SLS-process stage, we employ the non-isothermal phase-field model proposed in our former work[28] to simulate the coupled thermo-structural evolution, and perform the subsequent thermo-elasto-plastic calculations based on the resulting transient mesoscopic structure (hereinafter called mesostructure) and temperature field from the SLS simulations. In other words, mechanical stress and strain are developed under the quasi-static microstructure and temperature field. This is based on the fact that the thermo-mechanical coupling strength is negligible for most metals[32], unlike the strong inter-coupling among mass as well as heat transfer and grain growth[33,34]. From a kinetic point of view, the propagation of elastic waves is generally faster than thermal conduction and diffusion-based mechanisms, like grain coarsening and solid-state phase transition. Next, taking the nanoscopic domains that are sufficiently small and can be regarded as "homogenized points" on the mesostructure, we transfer the historical quantities on the sampled coordinates, notably the temperature and stress histories, to the subdomains as the transient uniform fields and perform the non-isothermal phase-field simulations of the γ/γ' transitions. This also means that mesoscopic temperature gradients are disregarded in the nanoscopic simulations in this work. Finally, we connect the nanoscopic Ni concentration (hereinafter as X_{Ni}) and stress field to the magnetic properties, incl. the saturation magnetization $M_s(X_{Ni})$, magneto-crystalline anisotropic strength $K_u(X_{Ni})$, and magnetostriction constants $\lambda_{100}(X_{Ni})$ and $\lambda_{111}(X_{Ni})$, and perform the magneto-elastic coupled micromagnetic simulations for the local hysteresis. Both non-isothermal phase-field and thermo-elasto-plastic models are numerically implemented by the finite element
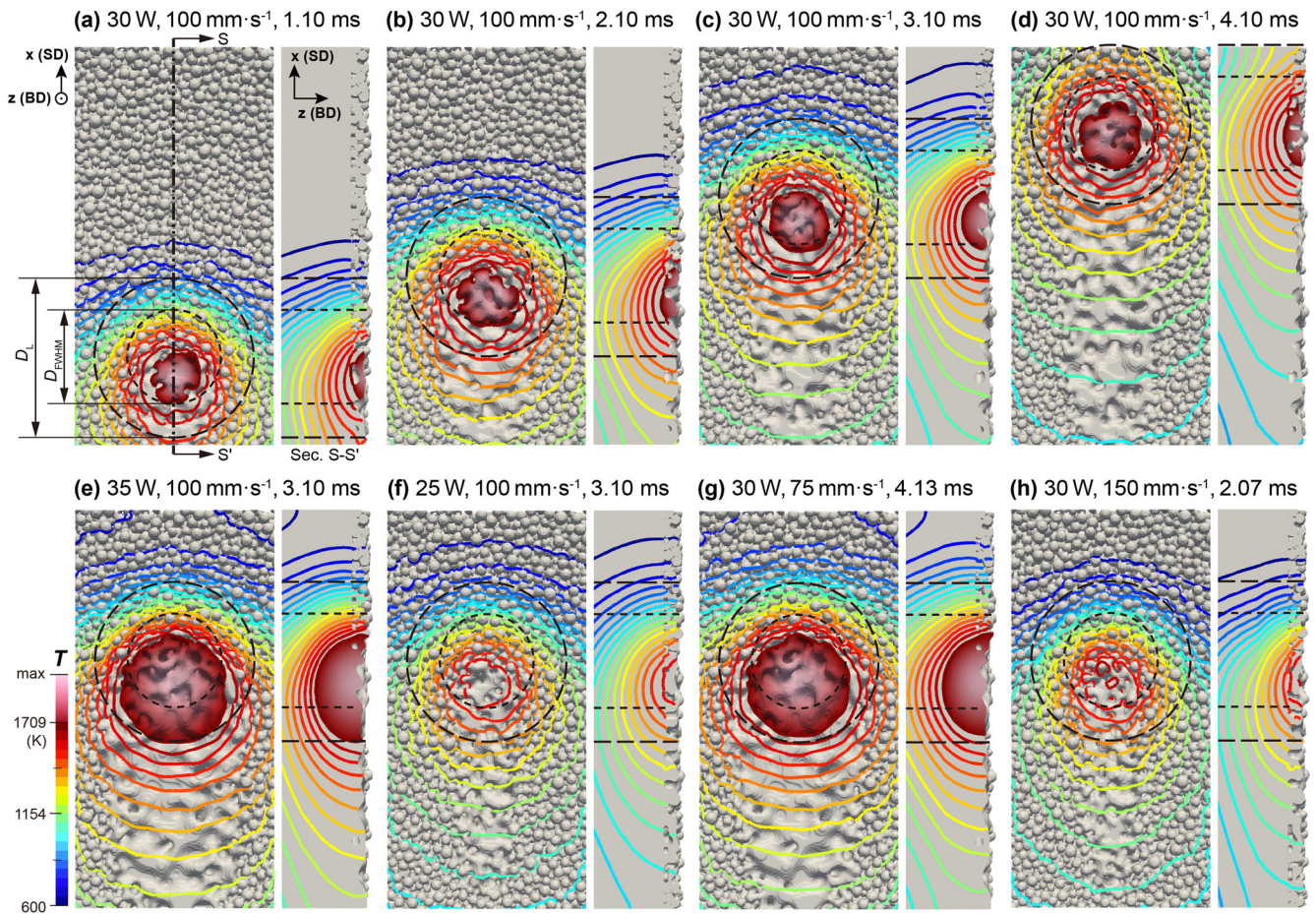
Fig. 3 Simulated thermal-microstructural evolution during SLS single scan. a–d SLS simulation results with beam power 30 W and scan speed 100 mm s^{-1} at different time points. **e–h** SLS simulation results with varying beam power and scan speed at the time point when the laser center locates at $x = 310$ µm. Fe$_{21.5}$Ni$_{78.5}$ is employed for both powder bed and substrate materials. Overheated regions, where $T > T_M$, are drawn with a continuous color map, while areas with $T \leq T_M$ are shown as isotherms. The laser spot characterized by D_L and D_{FWHM} is also indicated.

method (FEM), which allows handling the geometric complexity and adaptive meshing at considerable numerical accuracy. The micromagnetic models, on the other hand, are implemented by the finite difference method (FDM) to allow for GPU-accelerated high-throughput calculations[35]. Simulation domains are collectively illustrated in Supplementary Fig. 2. Apart from the main workflow, the proposed scheme also involves other methods, such as the discrete element method (DEM) and CALculation of PHAse Diagrams (CALPHAD) approach, to deliver information such as the powder size (R_i) and center (O_i) distributions and the thermodynamic/kinetic parameters that required in the simulations. Details regarding the modeling and the simulation setup are explicitly given in the *Method* section.

SLS single scan simulations and coupled thermal-microstructural evolution

Here we present the results of SLS single-scan simulations of a Fe$_{21.5}$Ni$_{78.5}$ powder bed in Argon atmosphere. A powder bed with an average thickness of $\bar{h} = 25$ µm is placed on a substrate with thickness of 240 µm and the same composition. The powder size distribution is presented in Supplementary Fig. 1b. The simulation domain has the geometry of $250 \times 500 \times 300$ µm. The melting point of Fe$_{21.5}$Ni$_{78.5}$ is $T_M = 1709$ K, and the initial temperature of the powder bed is set as the pre-heating/annealing temperature $T_0 = 0.351 T_M = 600$ K. The temperature at the substrate bottom is set as T_0 throughout the simulations. $D_{FWE2} = 200$ µm (i.e., full-

width at $1/e^2$) is adopted as the nominal diameter of the laser spot, within which around 86.5% of the power is concentrated. The full width at half maximum intensity (FWHM) is then calculated as $D_{FWHM} = 0.588 D_{FWE2} = 117.6$ µm, characterizing 50% power concentration within the spot.

Figure 3a–d shows the evolution of simulated microstructure for a single scan of $P = 30$ W and $v = 100$ mm s^{-1}. In the overheated region, particles may be fully/partially melted. The tendency to reduce the total surface energy leads to the motion of the localized melt flowing from convex to concave points, which contributes to the fusion of the powders. In regions with $T \leq T_M$, no melting occurs. However, the temperature of the particles is sufficiently high to induce diffusion, evidenced by the formation of necking between adjacent particles. Since the local temperature is well above the γ/γ' transition temperature during the SLS processes, there is no ordering at this stage.

The temperature profiles of the powder bed for different beam powers and scan speeds are presented in Fig. 3e–h, where the temperature field strongly depends on particle morphology, as the isotherms are concentrated around the surface concaves and sintering necks among particles. Apart from this, one can observe relatively dense isotherms at the front and the bottom of the overheated region, indicating a large temperature gradient. While the laser spot is moving, this temperature gradient becomes smaller, as the isotherms tend to be sparser. This indicates a fast heating process followed by slow cooling. Comparing the beam spot for different processing parameters presented in Fig. 3e–h
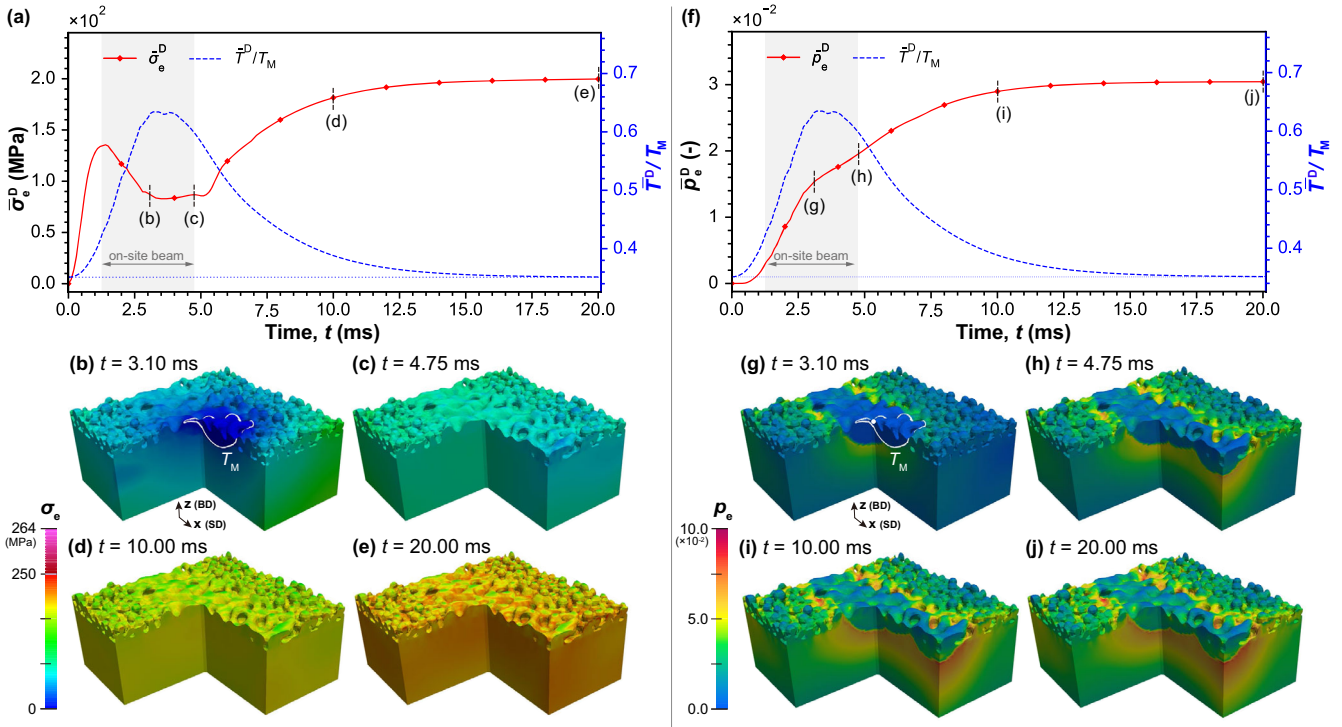
Fig. 4 Development of stress and plastic strain during SLS single scan. a Calculated von Mises stress ($\overline{\sigma}_e^D$) and temperature ($\overline{T}^D$) in domain average vs. time with the profile of σ_e at the denoted states shown in (**b–e**). **f** Calculated accumulated plastic strain in domain average ($\overline{p}_e^D$) vs. time with the profile of p_e at the denoted states shown in (**g–j**).

shows that increasing the beam power and/or decreasing the scan speed enhance the heat accumulation at the beam spot, resulting in the overheated region with increasing size. For the same scan speed $v = 100$ mm s^{-1}, increasing the beam power from $P = 30$ W (Fig. 3c) to 35 W (Fig. 3e) leads to more significant overheated region. On the other hand, for the same power of $P = 30$ W, increasing the scan speed from $v = 100$ mm s^{-1} (Fig. 3c) to 150 mm s^{-1} (Fig. 3h) leads to reduced overheated region.

Development of stress and plastic strain during SLS single scan

In order to analyze the stress evolution during SLS, we use isotropic hardening plasticity to describe Fe$_{21.5}$Ni$_{78.5}$ with temperature-dependent mechanical properties, including thermal expansion coefficient α, Young's modulus E, yield stress σ_y, and hardening tangent modulus E_t. The usage of the temperature-dependent isotropic mechanical properties is based on the observation of coexisting mesoscopic pores and nanoscopic in-grain solid-state γ' phase, which may sufficiently reduce the anisotropy due to the columnar polycrystalline texture by AM processing[36,37]. Nevertheless, the influences from AM-resulted polycrystalline texture on the thermo-elasto-plastic behaviors of the permalloy remain unclear and should be covered in future researches. Spatial interpolation of the mechanical properties according to the order parameter ρ, which is $\rho = 1$ in the materials and $\rho = 0$ in the atmosphere/pores, is also performed to consider structural inhomogeneities due to pore formation. Details are described in the section on *Methods*. The domain-average quantities are defined as

$$\overline{\sigma}_e^D = \frac{\int_\Omega \rho\sigma_e d\Omega}{\int_\Omega \rho d\Omega}, \qquad \overline{p}_e^D = \frac{\int_\Omega \rho p_e d\Omega}{\int_\Omega \rho d\Omega}, \qquad \overline{T}^D = \frac{\int_\Omega \rho T d\Omega}{\int_\Omega \rho d\Omega}, \qquad (1)$$

where Ω is the simulation domain volume, and ρ is the order parameter indicating the substance. σ_e is the von Mises stress and

p_e is the accumulated (effective) plastic strain. To eliminate the boundary effects, which lead to heat accumulation on the boundary that intersects with the scan direction, the simulation domain with a geometry $250 \times 250 \times 250$ μm is selected from the center of the domain for processing with the transient T and ρ fields mapped, as shown in Fig. 2.

Figure 4a presents the evolution of the domain-average von Mises stress during the SLS and cooling stages. σ_e develops with the temperature rise due to the generation of laser-induced heat in the powder bed. However, once the laser spot moves into the domain, followed by the overheated region, $\overline{\sigma}_e^D$ drops along with $\overline{T}^D$ continuing rising to the maximum. This is because the points inside the overheated region lose their stiffness, as the material is fully/partially melted, thereby presenting zero stress (Fig. 4b). Surroundings of the overheated region also present relatively low stress due to the sufficient reduction of stiffness at high temperatures. When the laser spot moves out of the domain, the thermal stress starts to develop along with the cooling of the domain (Fig. 4c–e). The stress around the concave morphologies on the powder bed, incl. concaves on the surface and sintering necks among particles, rises faster than the one around the traction-free convex morphologies on the surface and unfused powders away from the fusion zone. This may attribute to the locally high temperature gradient around the concave morphologies during the SLS process and, thereby, the strong thermal traction. At the end of the cooling, the convex morphologies and unfused powders have relatively lower stress developed, while the locally concentrated stress can be observed around the concave morphologies on the powder bed, like the surface concaves and sintering necks among particles (Fig. 4e). Due to the convergence of the σ_e vs. time in the cooling stage, the stress at the end of the cooling stage ($t = 20$ ms) will be regarded as the residual stress in the following discussions.

The development of the accumulated plastic strain p_e presents an overall increasing tendency vs. time during the SLS and cooling
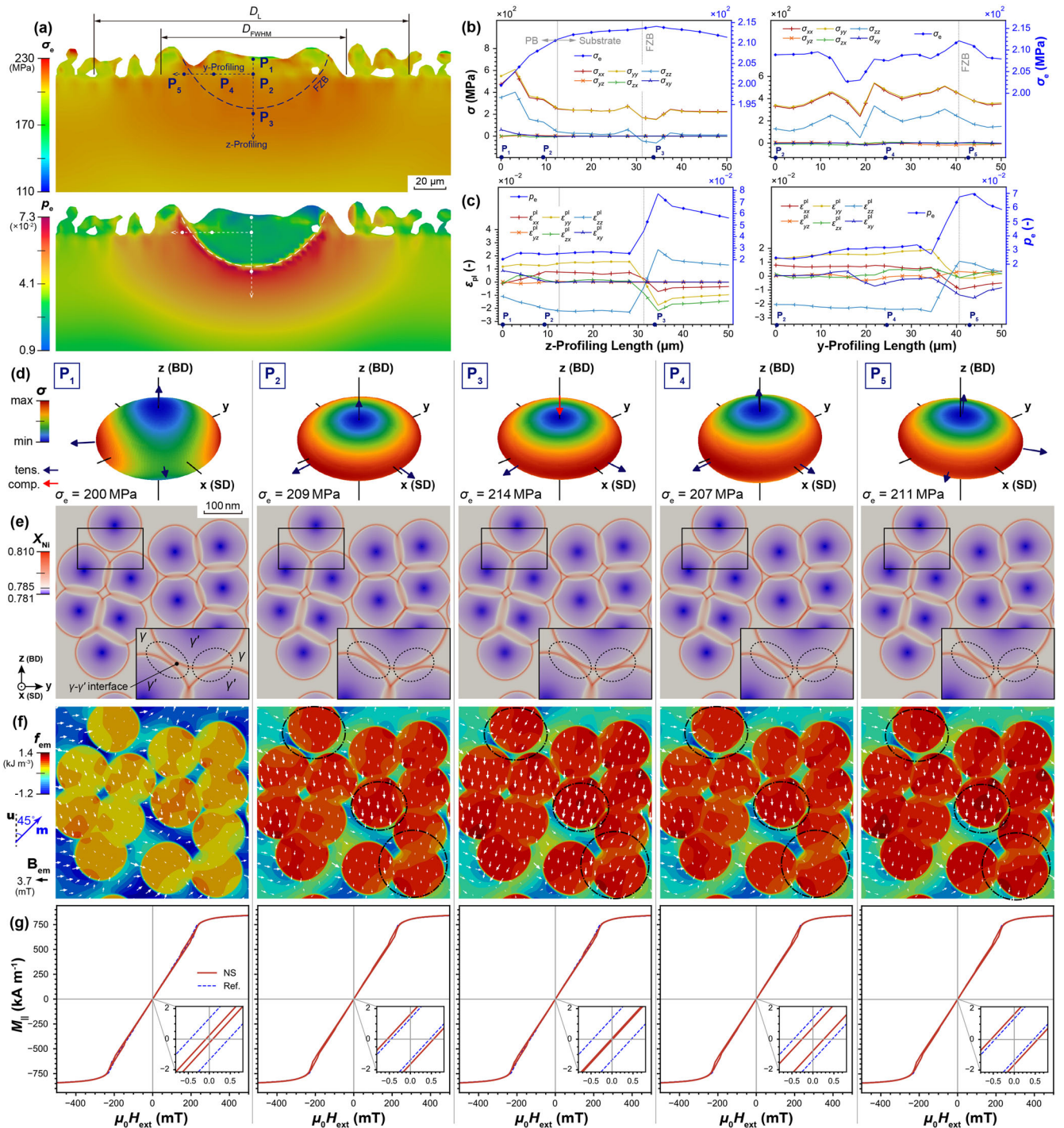
Fig. 5 γ/γ' transitions and magneto-elastic responses of stressed nanostructures. Profiles of (**a**) the von Mises residual stress σ_e and the accumulated plastic strain p_e on the middle section perpendicular to the x-direction (SD). The selected points P_1-P_5 are also indicated. The components and effective values of (**b**) the residual stress and (**c**) the plastic strain along the z- and y-profiling paths as indicated in (**a**). **d** The Lamé's stress ellipsoids, representing the stress state at P_1-P_5, are illustrated with the principal stresses denoted and colored (marine: tension; red: compression). **e** Ni concentration profile after annealing for 1200 h at $T_0 = 600K$ with the inset indicating the corresponding solid-state phases and the interface. **f** The magneto-elastic coupling energy f_{em} calculated under a homogeneous in-plane **m** configuration with $\vartheta = 45°$ w.r.t. the easy axis **u**. The effective coupling field B_{em} is also illustrated. **g** The average hysteresis loop of 10 cycles each performed on the nanostructures (NS) at P_1-P_5. The reference curve (ref.) is performed on the stress-free homogeneous nanostructure with only γ' phase and the composition $Fe_{21.5}Ni_{78.5}$.

stages, as shown in Fig. 4f. To emulate the effects of full/partial melting, we reset the p_e in the overheated region ($T > T_M$). This reset, however, does not influence the accumulation of p_e outside of the overheated region (Fig. 4g), distinguished from σ_e that

suffers reduction not only inside but also outside of the overheated region due to loss of stiffness at high temperature. As a result, the growth of the $\bar{p}_e^D$ slows down only when the laser spot moves into the domain rather than tends to reduce as $\bar{\sigma}_e^D(t)$.

The continuous accumulation of p_e also results in the distinctively concentrated p_e at the fusion zone's outer boundary (Fig. 4g–j), attributing to the high temperature gradient at the front and bottom of the overheated region during the SLS where the existing high thermal stress locally activates the plastic deformation and then contribute to the rise of the p_e. The same reason can be used to explain the concentrated p_e around the pores and concave morphologies like sintering neckings near the fusion zone. In contrast, unfused powders and substrate away from the fusion zone present nearly no accumulation of p_e, as the onsite thermal stress due to relatively low local temperature is not high enough to initiate the plastification of the material.

Nanoscopic γ/γ′ transition with residual stress

Before sampling many points inside the fusion zone for studying the subsequent γ/γ′ transition and carrying out micromagnetic simulations, we first examined five selected points from the middle section of the SLS simulation domain, counting its repeatability along the x-direction (SD). Profiles of σ_e and p_e are presented on this selected middle section in Fig. 5a. These five points are taken from the profiling path along z-direction (BD) and y-direction, as σ_e and p_e along these two paths are explicitly presented in Fig. 5b, c. σ_e gradually rises along z-profiling path, as the gap between the normal stresses (specifically between σ_{xx} and σ_{zz}, and between σ_{yy} and σ_{zz}) since there are almost no differences between σ_{xx} and σ_{yy}. σ_e reaches a peak around the fusion zone boundary (FZB) and then decreases. Notably, there is a reverse of σ_{zz} from positive (tension) to negative (compression) across the FZB. Similarly, p_e increases to a peak around the FZB and then decreases along z-profiling path, and the reversed components of $\boldsymbol{\varepsilon}_{pl}$ are observed across the FZB. This implies the bending of the SLS-processed mesostructure caused by the thermal contraction between the fusion zone and substrate, where the high temperature gradient is depicted. Along the y-profiling path, both σ_e and p_e present no monotonic tendencies, receiving influences from the morphologies, yet still reach peaks around the FZB, respectively.

The Lamé's stress ellipsoids are illustrated in Fig. 5d for visualizing the stress state of selected points with the directions of the principal stress denoted. Points near the surface and in the fusion zone (P_1, P_2, P_4, and P_5) are under tensile stress states, while the point P_3 near the FBZ has one negative principal stress (compressive) along BD due to the bending caused by the thermal contraction in the fusion zone. The Ni concentration and nanoscopic stress redistribution due to the γ/γ′ transition are simulated in the middle section perpendicular to SD as well (Supplementary Fig. 2c). It is also coherent with the diffuse-controlled 2D growth of γ′ phase experimentally examined by the Johnson-Mehl-Avrami-Kolmogorov (JMAK) theory[30]. We initiate the γ′ nuclei randomly but with a minimum spacing of 100 nm according to the experimental observation in Fig. 1c using Poisson disk sampling[38]. A relatively longer annealing time of 1200 h to obtain sufficient γ′ phase formation, as presented in Fig. 5e. The Ni concentration (X_{Ni}) at the centers of the grown γ′ phase is relatively low, close to the equilibrium value 0.764 at $T_{γ/γ'} = 766\,K$. With the growth of the γ′ phase, Ni is accumulated at the interface due to the relatively large γ/γ′ interface mobility compared with the inter-diffusive mobility of Ni species, agreeing with its diffuse-controlled growth examined experimentally[30]. Among the points, P_3 with one principal compressive stress has relatively larger γ′ grown after annealing. This is due to the growing γ′ phase with relatively smaller lattice parameters (in other words, inciting shrinkage eigenstrain inside γ′ phase) being mechanically preferred with compressive stress. As P_2 and P_5 with similar stress states, similar γ′ phase formations are shown. P_1 has relatively less γ′ phase grown, as it has the highest normal stresses as tensile (σ_{xx}, σ_{yy}, and σ_{zz}) compared to other points, as shown in Fig. 5b.

Magnetic hysteresis behavior of stressed nanostructures

The nanoscopic distributions of stress and Ni concentration are imported from the results of the γ/γ′ transition, in which both the long-range and short-range factors are embodied. The magneto-elastic coupling is implemented by considering an extra term f_{em} in the magnetic free energy density along with the exchanging, magneto-crystalline anisotropy, magnetostatic, and Zeeman contributions[31,39,40], as described in the section on *Methods*. To consider contributions from normal and shearing stresses, a homogeneous in-plane configuration for the normalized magnetization $\mathbf{m}$ is oriented in an angle of $\vartheta = 45°$ to the crystalline orientation $\mathbf{u}$, which is assumed to be the z-direction. Meanwhile, an effective coupling field $\mathbf{B}_{em} = -\partial f_{em}/\partial(M_s\mathbf{m})$ is calculated for analyzing the magneto-elastic coupling effects in vectorial aspect (Fig. 5f). It should be noted that within the range of segregated X_{Ni} from 0.781 to 0.810 as shown in Fig. 5e, λ_{100} ranges from 1.274×10^{-5} to 5.249×10^{-6}, presenting a positive shearing magnetostriction. On the other hand, λ_{111} inside of the γ′ phase ($X_{Ni} = 0.781 \sim 0.785$) and in the γ matrix ($X_{Ni} = 0.785$) has positive values, ranging from 2.41×10^{-6} to 1.96×10^{-6}, while X_{Ni} shifts from 0.781 to 0.785. On the γ/γ′ interface with $X_{Ni} = 0.810$, however, a negative value of $\lambda_{111} = -8.429 \times 10^{-7}$ is obtained. This implies that there is a negative normal magnetostriction on the γ/γ′ interfaces and a positive normal magnetostriction in the bulk of γ and γ′ phases. Due to the existing shrinkage eigenstrain, there are locally high f_{em} contributions inside the γ′ phase compared to the γ matrix, which causes strong magneto-elastic coupling effects. Among all points P_1-P_5, P_1 has comparably lower magneto-elastic coupling in both γ′ and γ phases. Owing to similar stress states, P_2, P_4, and P_5 have similar profiles of f_{em} and $\mathbf{B}_{em}$, where P_5 has slightly stronger coupling effects. Remarkably, P_2, P_4, and P_5 all have the local $\mathbf{B}_{em}$ lying at an angle about 135°, as emphasized by dashed-dotted circle Fig. 5f. As for P_3, however, the angle between $\mathbf{m}$ and $\mathbf{B}_{em}$ further increases to 142 to 165° together with larger magnitude ($|\mathbf{B}_{em}|$) comparing to other points, demonstrating enhanced reversal effects to the $\mathbf{m}$.

The hysteresis curves of the nanostructures also reflect the X_{Ni}-dependence of K_u, λ_{100} and λ_{111}. For comparison, the hysteresis curves simulated on a stress-free reference with a homogeneous $X_{Ni} = 0.785$ are also plotted. In order to take numerical fluctuations into account, ten cycles of the hysteresis were examined for each nanostructure/reference with the averaged one presented in Fig. 5g. Notice that K_u ranges from -0.137 to $-0.364\,kJ\,m^{-3}$ according to Fig. 1a, which can be regarded as the easy-plane anisotropy as the magnetization prefer to orient in the plane perpendicular to BD. Comparing selected points, P_2 and P_5 have similar coercivity, which is 0.55 mT for P_2 and 0.58 mT for P_5, as these two points have similar stress states. P_4 and P_1 have the coercivity of 0.26 mT and 0.09 mT, respectively. However, the coercivity at P_3 is infinitesimal. This is phenomenologically due to the strong coupling field $\mathbf{B}_{em}$ that reverses $\mathbf{m}$ at the relatively low external field, as shown in Fig. 5f. As the coupling field $\mathbf{B}_{em}$ is directly related to the stress state, the relatively strong shear stress implied by the Lamé's stress ellipsoids at P_3 (Fig. 5d) may be one of the reasons for the infinitesimal coercivity. This should be further examined in future studies.

DISCUSSION

It should notice that the size of the fusion is directly linked to the overheated region, which varies with the different combinations of beam power P and scan speed v, as shown in Fig. 3e–h. The usage of the conserved OP ρ in representing the powder bed morphologies and the coupled kinetics between ρ and local temperature allows us to simulate the formation of the fusion zone in a way close to the realistic setup of SLS. Here the indicator ξ is utilized to mark the fusion zone, which is initialized as zero and
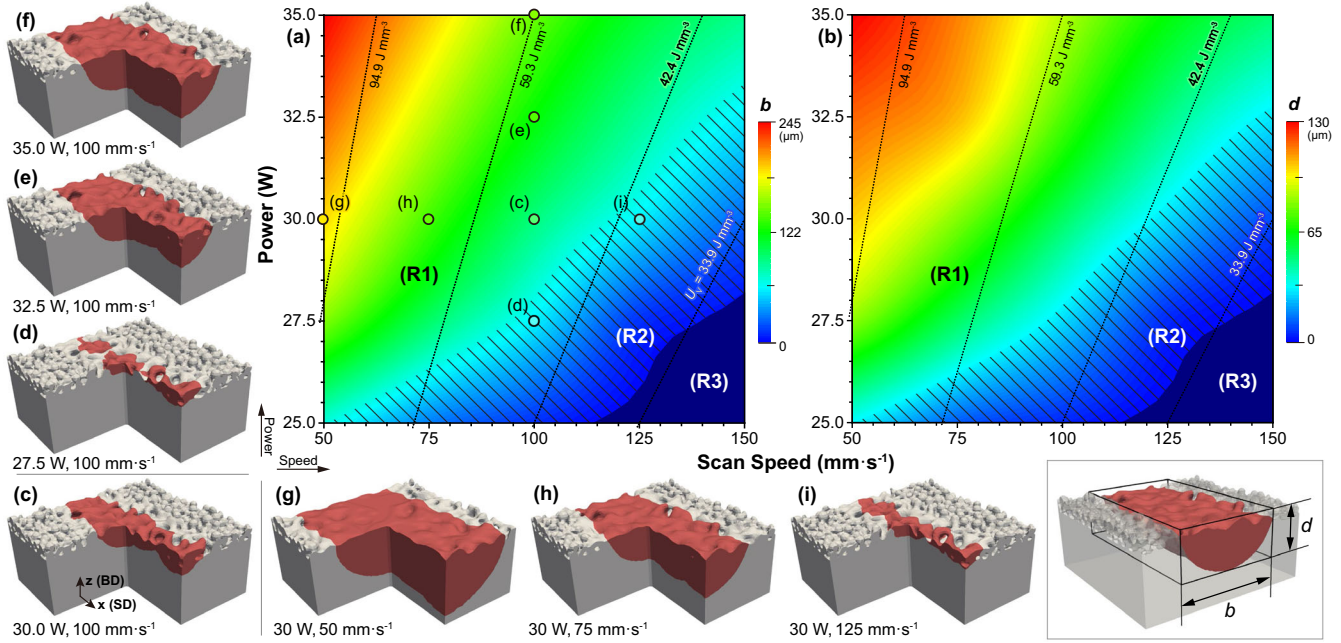
Fig. 6 Dependence of fusion zone geometry on processing parameters. Contour maps of (**a**) the width b and (**b**) the depth d of the fusion zone w.r.t. the beam power and the scan speed. The dotted lines represent isolines of specific energy input U_V. **c–i** Fusion zone geometries on the powder bed with different processing parameters. Inset: b and d measured from the fusion zone geometries.

would irreversibly turn to one once the temperature is above T_M[41]. Two characteristic sizes, namely the fusion zone width b and the fusion zone depth d, are defined by the maximum width and depth of the fusion zone, as shown in the inset of Fig. 6. Figure 6a and b present the maps of b and d vs. P and v, with the isolines indicating the identical volumetric specific energy input U_V that is calculated as

$$U_V = \frac{\eta P}{\bar{h} w v}, \tag{2}$$

where the width of the laser scan track w takes $D_{FWHM} = 117.6 \, \mu m$ and the average thickness of the powder bed $\bar{h} = 25 \, \mu m$. Since 50% total power is concentrated in the spot with D_{FWHM}, the efficiency takes $\eta = 0.5$. According to the observed geometry of the fusion zone, the maps can be divided into three regions: P and v located in the region (R1) would result in a continuous fusion zone, as shown in Fig. 6c, e–h. The depth of the fusion zone in (R1) normally penetrates the substrate, implying the formation of a considerable size of the overheated region, within which the melting-resolidification would take the dominant role. P and v located in the region (R2) generate small and discontinuous fusion zones, as two classical geometries as shown in Fig. 6d, i. Its limited size implies the typical partial melting and liquid-state sintering mechanism, as the melt flow is highly localized and can only help the bonding among a subset of powder particles. It is worth noting that these discontinuous fusion zones should attribute to the thermal inhomogeneity induced by local stochastic morphology rather than the mechanisms like the Plateau-Rayleigh instability and balling, where a significant melting phenomenon is required[42–44]. In the region labeled as (R3), no fusion zone is generated under the chosen P and v, and the solid-state sintering process remains dominant in the powder bed.

Figure 7a, b present the maps of average residual stress $\bar{\sigma}_e$ and plastic strain $\bar{p}_e$ inside the fusion zone vs. P and v, with the specific energy input U_V indicated. The average residual stress and plastic strain inside the fusion zone are calculated with the fusion zone

indicator ξ from the relations

$$\bar{\sigma}_e = \frac{\int_\Omega \xi \sigma_e d\Omega}{\int_\Omega \xi d\Omega}, \quad \bar{p}_e = \frac{\int_\Omega \xi p_e d\Omega}{\int_\Omega \xi d\Omega}. \tag{3}$$

Since the properties inside the fusion zone are focused, only the results with P and v located in the continuous fusion zones (R1) and discontinuous ones (R2) are selected and discussed. Generally, the increase of the $\bar{\sigma}_e$ follows the direction of increasing specific energy input U_V, leading to the enlargement of the fusion zone. In other words, increasing the size of the fusion zone receives larger contractions between itself and the substrate, leading to the rise of the residual stress inside the fusion zone, comparing Fig. 7c–e and c, f–g. It worth noting that $\bar{\sigma}_e$ presents a rapid increase on U_V below $120 \, J \, mm^{-3}$, as shown in Supplementary Fig. 3. When $U_V > 60 \, J \, mm^{-3}$, there is almost no increase in $\bar{\sigma}_e$, which is reflected as the sparse contours beyond the isoline $U_V = 60 \, J \, mm^{-3}$. This implies the saturation of residual stress in the fusion zone when U_V is sufficiently large, despite the fusion zone would continue enlarging along with the further increase of U_V.

The map of $\bar{p}_e$ presents a ridge at $P = 30 \, W$, which is different from the monotonic dependence of $\bar{\sigma}_e$ on U_V. This means the $\bar{p}_e$ reaches a minimum at $P = 30 \, W$ for every selected v. This may reflect the competition between enlarging fusion zone and the accumulation of plastic strain in the fusion zone. In the low-power range, the accumulation of plastic strain is slower than the growth of the fusion zone, as the $\bar{p}_e$ reduces along with increasing P. When $P > 30 \, W$, the accumulation of plastic strain is faster than the growth of the fusion zone, as the $\bar{p}_e$ increases along with increasing P. Interestingly, such a tendency is not observed in reducing v with fixing P, as the $\bar{p}_e$ always grows monotonically with decreasing v at every selected P.

Moreover, σ_e drastically rises across the former boundary between powder bed and substrate for all selected combinations of P and v, as shown in Fig. 7c–g. This is due to the different mechanical responses between the porous powder bed and homogeneous substrate to the thermal stress formed together with the overheated zone. As the size of the fusion zone enlarged,
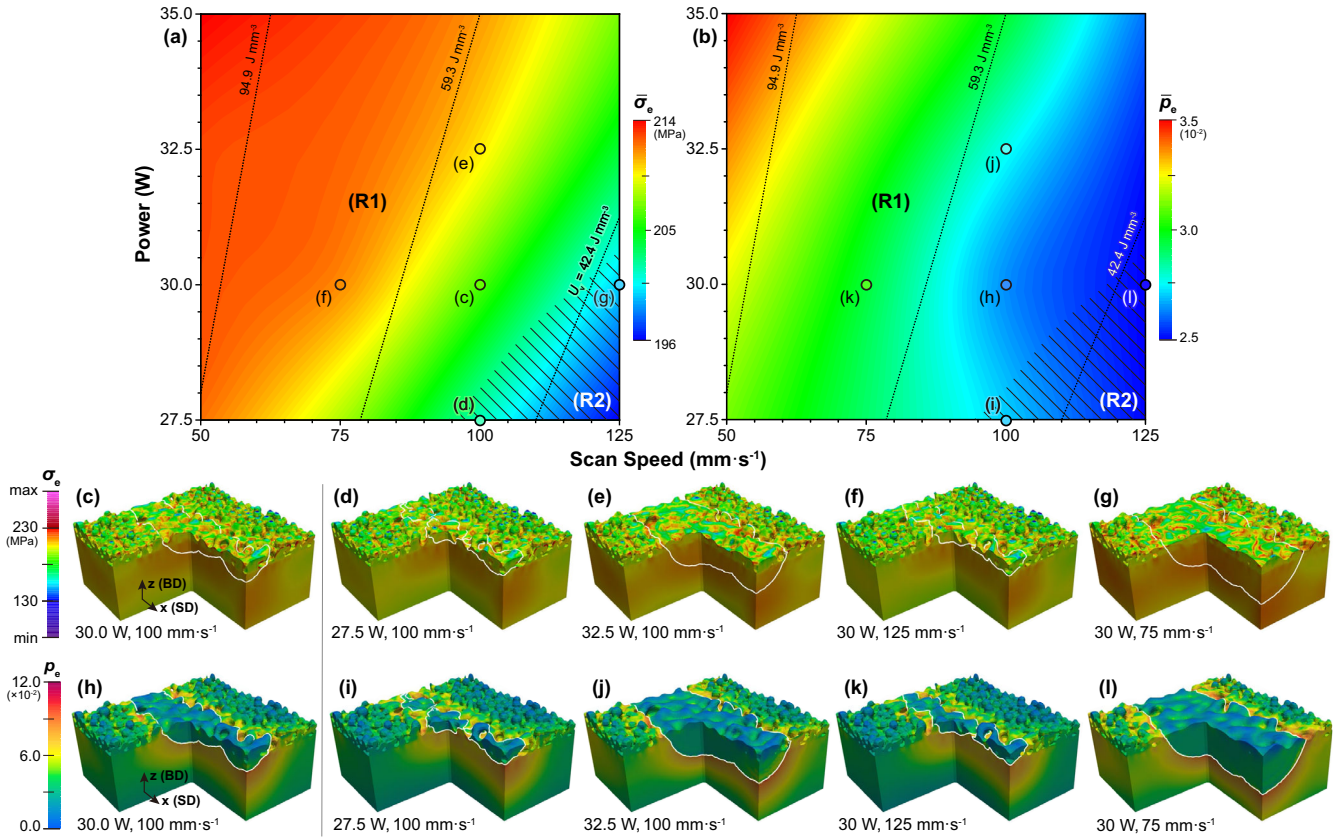
Fig. 7 Dependence of residual stress and plastic strain on processing parameters. Contour maps of (**a**) average residual stress $\overline{\sigma}_e$ and (**b**) average plastic strain $\overline{p}_e$ in the fusion zone w.r.t. the beam power and the scan speed. The dotted lines represent isolines of different specific energy inputs U_V. Profiles of (**c–g**) residual stress and (**h–l**) plastic strain are plotted for different processing parameters. The boundary of the fusion zone is also indicated.

the high concentration of σ_e extends further into the interior of the substrate, as the thermal contraction becomes enhanced between the fusion zone and the substrate. Meanwhile, a relatively low concentration of p_e is observed inside the fusion zone. And a relatively higher concentration is located at the fusion zone's outer boundary, reflecting the continuing accumulation of certain regions, as shown in Fig. 7h–l.

Many points located on the mid-section of the fusion zones were sampled, considering their repeatability along the x-direction (SD), as shown in Supplementary Fig. 4. It can also eliminate the boundary effects and distractions from the quantities outside the fusion zone. Nanoscopic γ/γ' transition and hysteresis simulations were performed on each point subsequently. Each hysteresis simulation applied the external magnetic field H_{ext} along the easy axis with identical loading history and increment size. After obtaining many longitudinal hysteresis curves $M_{\parallel}^I(H_{ext})$ with the point index I, the average hysteresis curve $\overline{M}_{\parallel}(H_{ext})$ is then calculated directly as the point-wise average of the resulting local hysteresis, i.e.,

$$\overline{M}_{\parallel}(H_{ext}) = \sum_N^I M_{\parallel}^I(H_{ext})/N, \qquad (4)$$

where N is the amount of sampled points. And the average characteristics, like average coercivity $\overline{H}_c$, were extracted from the averaged curve. Employing an identical sampling grid size, this averaged hysteresis can be statistically regarded as a collective outcome of many ferromagnetic pseudo-particles with their magnetization rotation individually dependent on the local nanoscopic phase formation, stress state, and applied magnetic field[45]. At least three hysteresis cycles were performed on each point to reduce the fluctuations due to the numerical scheme. In Fig. 8a, we present the average coercivity $\mu_0\overline{H}_c$ map with respect to the P and v. μ_0 is the vacuum permeability. In the map, the lower-right region shows a smaller coercivity, and the upper-left region shows a higher coercivity. Increasing P from 27.5 to 35 W results in the rise of $\mu_0\overline{H}_c$ from 0.35 to 0.41 mT (by 17%) when $v = 100$ mm s^{-1}, and decreasing v from 125 to 50 mm s^{-1} results in the rise of $\mu_0\overline{H}_c$ from 0.34 to 0.44 mT (by 29%) when $P = 30$ W. This is mainly due to the increasing fraction of region with high local coercivity in the fusion zone for increasing P and decreasing v (comparing Fig. 8c, d, e, c, f, g, respectively). It is also evident that the high local H_c points possess a high local volume fraction of γ' phase $\Psi_{\gamma'}$ (comparing Fig. 8c–g with h–l). This implies an enhanced magneto-elastic coupling effect at high $\Psi_{\gamma'}$, as discussed in Fig. 5f. However, the effect from the local residual stress on the pattern of high local H_c region should also be stressed, as the points with low local μ_0H_c around where the local σ_e has a drastic change, e.g., the former boundary between powder bed and substrate, comparing (Fig. 8c–g with m–q, especially 8e with o and f and p). Moreover, it remains unclear for the existing "islands" of low local H_c located in the high local σ_e and $\Psi_{\gamma'}$ region. They may be subject to a stress state similar to the P_3 in Fig. 5 where nearly zero coercivity is obtained. Nonetheless, a data-driven investigation should be conducted as one upcoming work to connect the local stress state to the coercivity. Other average characteristics like the remnant $\overline{M}_r$ and the saturation magnetization $\overline{M}_s$ are also correspondingly read from the average hysteresis curve $\overline{M}_{\parallel}(H_{ext})$ and presented in Supplementary Fig. 10. Interestingly, $\overline{M}_r$ presents a nearly identical distribution as $\mu_0\overline{H}_c$ vs. P and v, and increases following the direction of rising specific energy input. $\overline{M}_s$, however, presents an inversed distribution vs. P and v and a decreasing tendency with respect to the dropping specific energy
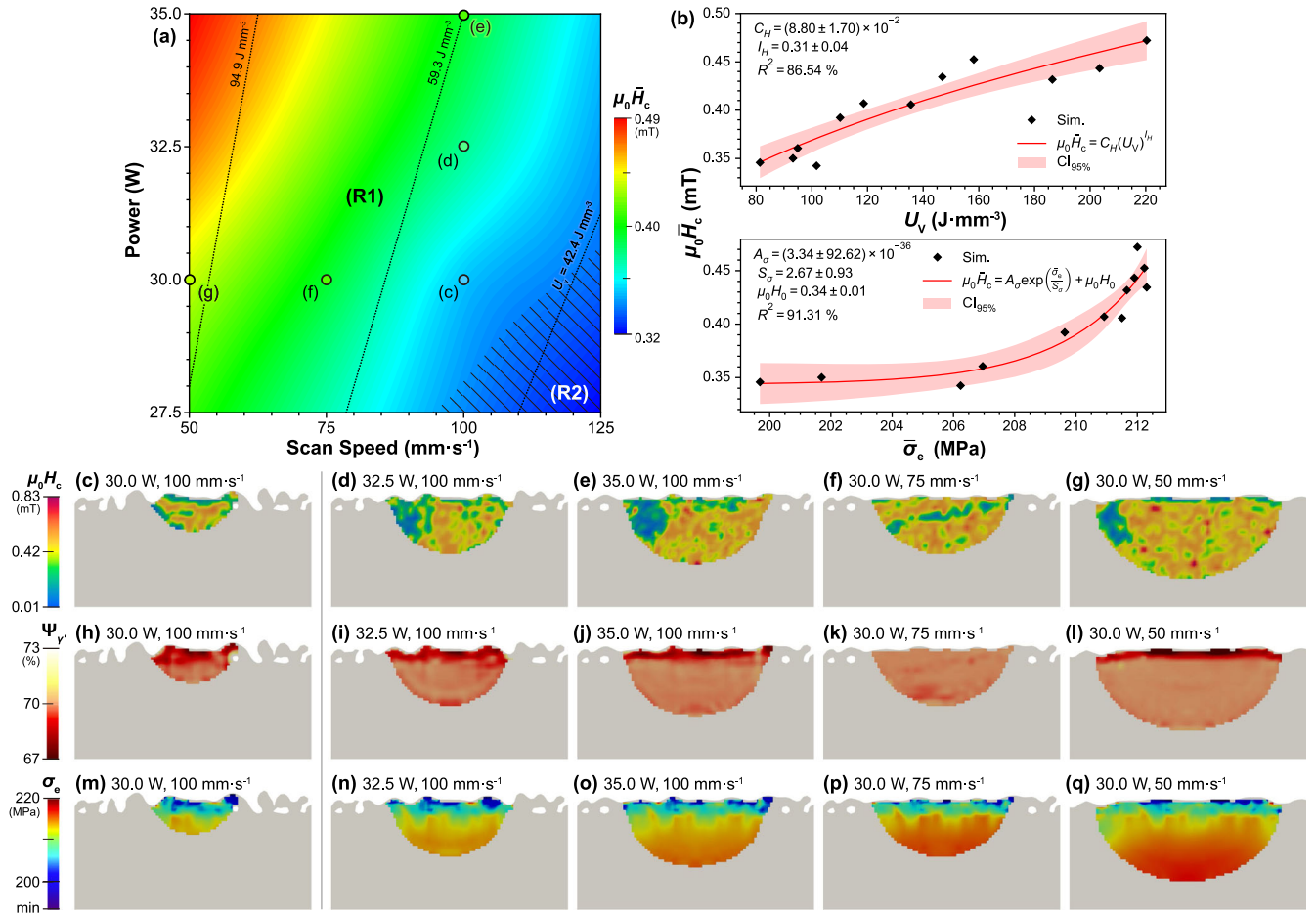
Fig. 8 Dependence of magnetic coercivity on processing parameters. a Contour map of the average coercivity $\mu_0\overline{H}_c$ in the fusion zone w.r.t. the beam power and the scan speed. The dotted lines represent different specific energy input isolines U_V. **b** Nonlinear regression of $\mu_0\overline{H}_c$ on specific energy input U_V and average residual stress $\overline{\sigma}_e$, with the regression parameters indicated correspondingly. It presents that $\mu_0\overline{H}_c$ subjects to scaling rule on U_V and to exponential growth law on $\overline{\sigma}_e$ with the correlation coefficient $R^2 = 86.54\%$ and 91.31%, respectively. Profiles of (**c–g**) the local coercivity; (**h–l**) the local volume fraction of γ' phase; and (**m–q**) the local residual stress on the mid-sections of the fusion zones are plotted for different processing parameters.

input, even though its variation limits in a narrow range, i.e., 854.82 to 854.92 kA m^{-1}.

To examine the dependence of $\mu_0\overline{H}_c$ on the processing parameters from the phenomenological aspect, we performed the nonlinear regression analysis of $\mu_0\overline{H}_c$ on the specific energy input U_V. The results are presented in Fig. 8b. Notably, $\mu_0\overline{H}_c$ relates to U_V by allometric scaling rule, i.e., $\mu_0\overline{H}_c = C_H(U_V)^{I_H}$ with C_H and I_H the parameters. The analysis gives the correlation coefficient $R^2 = 86.54\%$ with relatively large uncertainty located on low and high U_V regions. Regressed $I_H = 0.31 \pm 0.03$ also implies a diminishing scaling of $\mu_0\overline{H}_c$ by U_V, as the increment of $\mu_0\overline{H}_c$ decreases with the increase of U_V. However, similar to the one for $\overline{\sigma}_e$, such a simple scaling rule between the specific energy input and coercivity might be challenged since U_V may not be able to identify the uniquely H_c for the SLS-processed part, as the isoline of U_V in Fig. 8a evidently intersects with the contour of $\mu_0\overline{H}_c$.

Regression analysis of $\mu_0\overline{H}_c$ on σ_e was also performed. The exponential growth rule was chosen based on the tendency of $\mu_0\overline{H}_c(\overline{\sigma}_e)$, i.e., $\mu_0\overline{H}_c = A_\sigma \exp\left(\frac{\overline{\sigma}_e}{S_\sigma}\right) + \mu_0H_0$ with A_σ, S_σ and H_0 as the parameters. Here we adopt the A_σ as the growth pre-factor and S_σ as the stress scale. When $\overline{\sigma}_e = 0$, we have $\mu_0H_c|_{\overline{\sigma}_e=0} = A_\sigma + \mu_0H_0 \approx \mu_0H_0$, meaning μ_0H_0 can be regarded as the stress-free coercivity. The analysis gives a relatively higher correlation coefficient $R^2 = 91.31\%$ cf. the one on U_V, with relatively large

uncertainty located on low U_V region. Compared to the homogeneous stress-free reference in Fig. 5g that is 0.45 mT, this μ_0H_0 is around 24% smaller, owing to the contributions from the infinitesimal-coercivity points. It also presents the rapid growth of $\mu_0\overline{H}_c$ after $\overline{\sigma}_e = 206$ MPa with around 40% increment, demonstrating evident effects on $\mu_0\overline{H}_c$ with increasing residual stress.

In summary, the processing-property relationship in tailoring magnetic hysteresis of $Fe_{21.5}Ni_{78.5}$ has been demonstrated in this work by conducting multiphysics-multiscale simulation. The residual stress is unveiled to be the key thread since it readily carries both long-range (morphology and morphology-induced chronological-spatial thermal inhomogeneity) and short-range information (misfit-induced fluctuations) after the processes. Influences of beam power and scan speed have been investigated and presented on distinctive phenomena, including the geometry of fusion zones, the residual stress and accumulated strain, and the resultant coercivity of the manufactured parts. The following conclusions can be drawn from the present work:

(i)   The simulated mesoscopic residual stress states are coherent with TGM interpretation. Further details like the concentrated stress around the concave morphologies (surface concave, sintering necks, etc) beyond the TGM interpretation are also delivered. The accumulated plastic strain is evidently observed at the fusion zone's outer boundary.
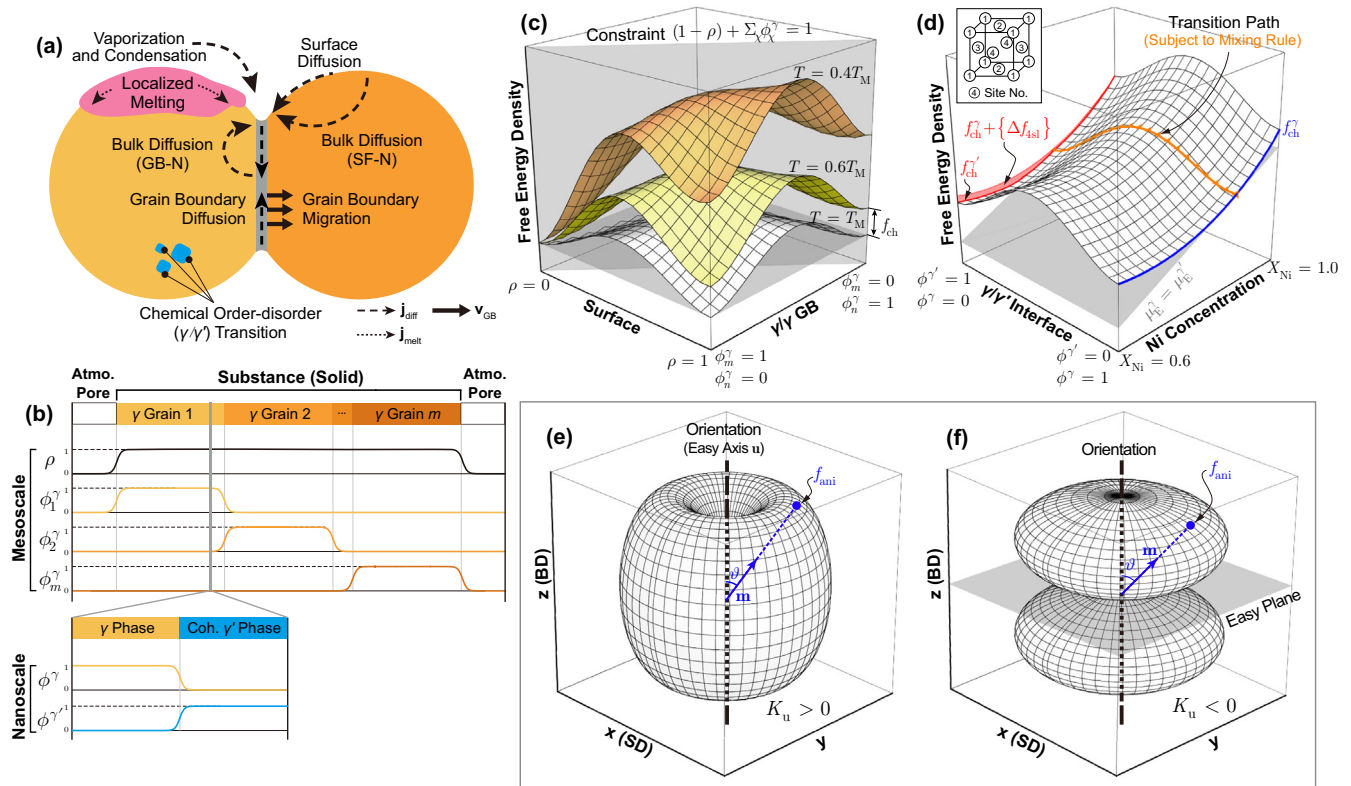
Fig. 9 Phase-field scenario and landscapes of free energy density. a Schematic of the physical processes during SLS, i.e., localized melting, multiple mass transfer paths, and grain boundary migration. Here, the bulk diffusion GB-N represents the path from grain boundary to neck through the bulk, while SF-N presents the path from the surface to neck through the bulk. **b** Profiles of different OPs across solid-state phases with the corresponding scales. **c** The landscape of mesoscopic stress-free f_{tot} across the surface and the γ/γ grain boundaries at various temperatures. **d** The landscape of nanoscopic stress-free f_{tot} across the γ/γ' coherent interface at 600 K. Transition path, f_{ch}^{γ}, $f_{ch}^{\gamma'}$, and the energy band of the four-sublattice states $\{\Delta f_{4sl}\} = \{f_{4sl}(Y^{(s)}) - f_{4sl}(Y^{(s)} = X^{\gamma'})\}$ are also denoted. Inset: sublattice sites for the L1$_2$ ordering of Fe-Ni. **e–f** Energy surface of magneto-crystalline anisotropy energy, which alters w.r.t. the sign of anisotropy constant K_u, i.e., (**e**) the easy-axis anisotropy when $K_u > 0$ and (**f**) the easy-plane anisotropy when $K_u < 0$.

(ii) Nanoscopic Ni segregation at the γ/γ' interface due to the diffusion-controlled γ/γ' transitions is observed with local composition Fe$_{19}$Ni$_{81}$, which has comparably smaller saturation magnetization and stronger easy-plane magnetocrystalline anisotropy. Notably, the interface also locally presents negative normal magnetostriction ($\lambda_{111} = -8.429 \times 10^{-7}$) and positive shearing magnetostriction ($\lambda_{100} = 5.249 \times 10^{-6}$), while both the γ' phase and γ matrix present positive normal and shearing magnetostriction.

(iii) Large magneto-elastic coupling energy is observed inside γ' phase with the corresponding effective field imposing rotating effects on the magnetization. These effects vary point-wisely according to residual stress states and γ' phase formation, and eventually lead to different local coercivity. Remarkably, the point around the bottom of the fusion zone is examined to have nearly zero coercivity, which may attribute to the on-site stress state with a principal compressive stress along the building direction with another two tensile ones, i.e., implying a relatively significant shear stress.

(iv) The relation between the average residual stress and coercivity of the fusion zone is examined to follow the exponential growth rule with a correlation coefficient of 91.31%. The stress-free coercivity derived from the exponential law is 0.34 mT, and the rapid growth of average coercivity is observed when average residual stress exceeds 206 MPa, implying a potential threshold of average residual stress for restricting coercivity of the manufactured parts around the stress-free value. On the other hand, average residual stress beyond the threshold can be considered in the context of

effectively increasing the resultant coercivity of the manufactured permalloy parts.

Despite the present findings, several points should be further examined and discussed in future works:

(i) The conditions deriving the near-zero coercivity should be extensively investigated in the sense of residual stress states rather than its effective value, noting that residual stress is a 2nd-order tensor. Magneto-elastic coupled micromagnetic simulations should be performed under the classified residual stress states to rationalize the factors leading to the vanishing coercivity as in the present findings.

(ii) The present findings are only examined at relatively low specific energy input and, correspondingly, low generated residual stress, as the SLS is chosen in this work. It is anticipated to conduct the simulations with relatively high energy input, like SLM, and examine the influences of magneto-elastic coupling on the magnetic hysteresis with comparably higher residual stress cases. Influences on residual stress development and, eventually, the coercivity of manufactured permalloy from multilayer and multitrack AM strategies should also be examined.

METHODS

Thermodynamic framework

In order to describe the microstructure of an SLS-manufactured Fe-Ni alloy, a conserved order parameter (OP) ρ is employed to

represent the substance and atmosphere/pores, and a set of non-conserved OPs $\{\phi_\chi^\varphi\}$ are employed to represent the grains with the superscript $\varphi = \gamma, \gamma'$ representing the phases and the subscript $\chi = 1, 2, ..., N$ representing the orientations, extended from our former works[28,33]. Counting the thermal, chemical, and mechanical contributions, the temperature field T, the strain field $\boldsymbol{\varepsilon}$, and sets of local chemical molar fraction $\{X_A^\varphi\}$ of the chemical constituents $A = \mathrm{Fe, Ni}$ are considered. On the other hand, as a ferromagnetic material under the Curie temperature $T_C = 880$ K for the composition $\mathrm{Fe}_{21.5}\mathrm{Ni}_{78.5}$, the thermodynamic contribution due to the existing spontaneous magnetization $\mathbf{m}$ is also counted. The framework of the free energy density functional of the system is then formulated as follows

$$\mathcal{F} = \int_\Omega \left[f_{\mathrm{ch}} + \overbrace{f_{\mathrm{loc}} + f_{\mathrm{grad}}}^{f_{\mathrm{intf}}} + f_{\mathrm{el}} + f_{\mathrm{mag}} \right] \mathrm{d}\Omega, \tag{5}$$

where f_{ch} represents the contributions from the chemical constituents. f_{loc} and f_{grad}, together as the f_{intf}, presents the contributions from the surface and interfaces (incl. grain boundaries and phase boundaries)[46]. f_{el} is the contribution from the elastic deformation, and f_{mag} is the contribution from spontaneous magnetization and magnetic-coupled effects.

It is worth noting that this uniform thermodynamic framework does not imply that a single vast inter-coupled problem with all underlining physics should be solved interactively and simultaneously crossing all involved scales. As sufficiently elaborated in the subsection *Multiphysics-multiscale simulation scheme*, it is more practical and effective to conduct the multiphysics-multiscale simulations in a subsequent scheme and concentrate on rationalizing and bridging the physical quantities and processes among problems and scales. In that sense, the free energy density functional, originated from Eq. (5), should be sufficiently simplified regarding the distinctiveness of each problem at the corresponding scale. This will be explicitly introduced in the following sections.

Mesoscopic processing simulations
Here we consider the SLS processing on a mesoscopic powder bed by using ρ to differentiate pore-substance and $\{\phi_\chi^\varphi\}$ to differentiate polycrystalline orientations. According to the high-temperature phase diagram of the Fe-Ni system[47], the γ phase exists within a relatively large temperature range (from $T_M = 1709$ K to the transition starting temperature $T_{\gamma/\gamma'} = 766$ K) for the composition $\mathrm{Fe}_{21.5}\mathrm{Ni}_{78.5}$. On the other hand, since the SLS together with cooling stages would only last a relatively infinitesimal time (on the order of 10 ms) to the following annealing stage (more than 10 h), there is almost no change for γ' phase to grow into mesoscopic size. In this regard, we treat all existing polycrystals during the SLS stage as the γ phase. Considering Fe-Ni as a binary system where the constraints $X_{\mathrm{Ni}} + X_{\mathrm{Fe}} = 1$ and $\phi_\chi^{\gamma'} + \phi_\chi^\gamma = \rho$ always holds, we then only take the OP set $\{\phi_\chi^\gamma\}$ ($\chi = 1, 2, ..., N$) as well as ρ for the mesoscopic simulations due to the absence of the γ' phase on the mesostructures. The profiles of ρ and $\{\phi_\chi^\gamma\}$ across the surface and grain boundary between two adjacent γ-grains are illustrated in Fig. 9b. We also take simplified notations $X = X_{\mathrm{Ni}}$ in this subsection as the independent concentration indicators, while $X_{\mathrm{Fe}} = 1 - X$.

Due to the co-existence of substance (γ-grains with Ni composition $X_0 = 0.785$) and pores/atmosphere, the chemical free energy density should be formulated as

$$f_{\mathrm{ch}}(T, \rho) = h_{\mathrm{ss}}(\rho)f_{\mathrm{ch}}^\gamma(T, X^\gamma = X_0) + h_{\mathrm{at}}(\rho)f_{\mathrm{ch}}^{\mathrm{at}}(T), \tag{6}$$

where h_{ss} and h_{at} are monotonic interpolation functions with subscripts "ss" and "at" representing the substance and pore/

atmosphere and are assumed to have the polynomial forms as

$$h_{\mathrm{ss}}(\rho) = \rho^3(10 - 15\rho + 6\rho^2), \quad h_{\mathrm{at}}(\rho) = 1 - \rho^3(10 - 15\rho + 6\rho^2).$$

The temperature-dependent chemical free energy f_{ch}^γ is modeled by the CALPHAD approach

$$f_{\mathrm{ch}}^\gamma = f_{\mathrm{ref}}^\gamma + f_{\mathrm{id}}^\gamma + f_{\mathrm{mix}}^\gamma + f_{\mathrm{mm}}^\gamma, \tag{7}$$

with

$$\begin{aligned}
f_{\mathrm{ref}}^\gamma(T, X^\gamma) &= X^\gamma f_{\mathrm{Ni}}(T) + (1 - X^\gamma)f_{\mathrm{Fe}}(T), \\
f_{\mathrm{id}}^\gamma(T, X^\gamma) &= \frac{\mathcal{R}T}{V_{\mathrm{m}}^{\mathrm{sys}}}[X^\gamma \ln X^\gamma + (1 - X^\gamma)\ln(1 - X^\gamma)], \\
f_{\mathrm{mix}}^\gamma(T, X^\gamma) &= X^\gamma[1 - X^\gamma]L^\gamma(T), \\
f_{\mathrm{mm}}^\gamma(T, X^\gamma) &= \frac{\mathcal{R}T}{V_{\mathrm{m}}^{\mathrm{sys}}}\ln(\beta^\gamma + 1)\mathbb{P}\left(\frac{T}{T_C^\gamma}\right),
\end{aligned}$$

where f_{ref}^γ is the term corresponding to the mechanical mixture of the chemical constituents (in this case, Fe and Ni), f_{id}^γ is the contribution from the configurational entropy for an ideal mixture, f_{mix}^γ is the excess contribution due to mixing, and f_{mag}^γ is the contribution due to the magnetic moment. The parameters fed in Eq. (7), including the atom magnetic moment β^γ, the Curie temperature T_C^γ, and the interaction coefficient L^γ, are described in the way of Redlish-Kister polynomials[48] which is generally formulated for a binary system as $p^\varphi = X_A p_A^\varphi + X_B p_B^\varphi + X_A X_B \sum_n p_{A,B}^{\varphi,n}(X_A - X_B)^n$ with the temperature-dependent parameters p_A^φ, p_B^φ and $p_{A,B}^{\varphi,n}$ for optimization. $\mathbb{P}(T/T_C^\gamma)$ represents the Inden polynomial, obtained by expanding the magnetic specific heat onto a power series of the normalized temperature T/T_C^γ[49,50]. $\mathcal{R}$ is the ideal gas constant. $V_{\mathrm{m}}^{\mathrm{sys}}$ is the molar volume of the system. All the thermodynamic parameters for the CALPHAD are obtained from ref. [47] while the molar volume of the system is obtained from the database TCFE8 from the commercial software Thermo-Calc®[51].

Since the variation of Ni composition is negligible in between T_M and $T_{\gamma/\gamma'}$, we pursue a simple but robust way of implementing f_{ch} under a drastically varying T during the SLS stage. Taking T_M as referencing temperature, Eq. (6) is then re-written as

$$f_{\mathrm{ch}}(T, \rho) = c_r\left[(T - T_M) - T\ln\frac{T}{T_M}\right] + f_{\mathrm{ref}}^{T_M} - h_{\mathrm{ml}}\frac{T - T_M}{T_M}\mathcal{L}, \tag{8}$$

where $f_{\mathrm{ref}}^{T_M}$ is a referencing chemical free energy density at T_M, which can be omitted in the following calculations. c_r is a relative specific heat landscape, i.e., $c_r(\rho, T) = h_{\mathrm{ss}}(\rho)c_v^\gamma(T) + h_{\mathrm{at}}(\rho)c_v^{\mathrm{at}}(T)$ with the volumetric specific heat for γ grains and pores/atmosphere. Notably, c_v^γ can be thermodynamically calculated as follows at a fixing pressure p_0 and composition X_0.

$$c_v^\gamma(T) = -T\left(\frac{\partial^2 f_{\mathrm{ch}}^\gamma}{\partial T^2}\right)_{p_0, X_0}. \tag{9}$$

It should be noticed that the c_v^γ obtained by Eq. (9) has a discontinuous point at T_C, which is due to the 2nd-order Curie transition, as shown in Supplementary Fig. 5a. $\mathcal{L}$ is the latent heat due to the partial/full melting, which is mapped by the interpolation function h_{ml}. Here h_{ml} adopts a sigmoid form with a finite temperature band Δ_T

$$h_{\mathrm{ml}} = \frac{1}{2}\left[1 + \tanh\frac{2(T - T_M)}{\Delta_T}\right].$$

which reaches unity once $T \to T_M$ and is smooth enough to ease the drastic change in f_{ch}.

On the other hand, to explain the free energy landscape across the surface and γ/γ interface (or γ grain boundary) under varying temperatures, we adopt the non-isothermal multi-well Landau

polynomial and gradient terms from our former works[28,33], i.e.,

$$
\begin{aligned}
f_{\text{loc}}(T, \rho, \{\phi_X^\gamma\}) &= \underline{W}_{\text{sf}}(T)\left[\rho(1-\rho)^2\right] + \underline{W}_{\gamma/\gamma}(T)\left\{\rho^2 + 6(1-\rho)\sum_X (\phi_X^\gamma)^2 \right. \\
&\qquad \left. -4(2-\rho)\sum_X (\phi_X^\gamma)^3 + 3\left[\sum_X (\phi_X^\gamma)^2\right]^2\right\}, \\
f_{\text{grad}}(T, \nabla\rho, \{\nabla\phi_X^\gamma\}) &= \tfrac{1}{2}\left[\underline{\kappa}_{\text{sf}}(T)|\nabla\rho|^2 + \sum_X \underline{\kappa}_{\gamma/\gamma}(T)|\nabla\phi_X^\gamma|^2\right],
\end{aligned}
$$

(10)

with

$$
\begin{aligned}
\underline{W}_{\text{sf}}(T) &= W_{\text{sf}}\tau_{\text{sf}}(T), & \underline{\kappa}_{\text{sf}}(T) &= \kappa_{\text{sf}}\tau_{\text{sf}}(T), \\
\underline{W}_{\gamma/\gamma}(T) &= W_{\gamma/\gamma}\tau_{\gamma/\gamma}(T), & \underline{\kappa}_{\gamma/\gamma}(T) &= \kappa_{\gamma/\gamma}\tau_{\gamma/\gamma}(T),
\end{aligned}
$$

$\underline{W}_{\gamma/\gamma'}$ and $\underline{\kappa}_{\gamma/\gamma'}$ are temperature-independent parameters obtained from the surface and γ/γ interface energy Γ_{sf}, $\Gamma_{\gamma/\gamma}$ and diffuse-interface width $\ell_{\gamma/\gamma}$, and $\tau_{\text{sf}}(T)$ and $\tau_{\gamma/\gamma}(T)$ are the dimensionless tendencies inherited from the temperature dependency of Γ_{sf} and $\Gamma_{\gamma/\gamma}$, i.e.,

$$
\begin{aligned}
\Gamma_{\text{sf}}(T) &= \tfrac{\sqrt{2}}{6}\tau_{\text{sf}}(T)\sqrt{(W_{\text{sf}} + 7W_{\gamma/\gamma})(\kappa_{\text{sf}} + \kappa_{\gamma/\gamma})}, \\
\Gamma_{\gamma/\gamma}(T) &= \tfrac{2\sqrt{3}}{3}\tau_{\gamma/\gamma}(T)\sqrt{W_{\gamma/\gamma}\kappa_{\gamma/\gamma}}, \\
\ell_{\gamma/\gamma} &\approx \tfrac{2\sqrt{3}}{3}\sqrt{\tfrac{\kappa_{\gamma/\gamma}}{W_{\gamma/\gamma}}},
\end{aligned}
$$

(11a)

along with the constraint among parameters for having the sample profile of ρ and ϕ_X^γ across the surface[28], i.e.,

$$
\frac{W_{\text{sf}} + W_{\gamma/\gamma}}{\kappa_{\text{sf}}} = \frac{6W_{\gamma/\gamma}}{\kappa_{\gamma/\gamma}}.
$$

(11b)

In this work, we give $\ell_{\gamma/\gamma} = 2\,\mu\text{m}$, the temperature-dependent Γ_{sf} and $\Gamma_{\gamma/\gamma}$ are presented in Supplementary Fig. 5c. The total free energy density landscape at stress-free condition ($f_{\text{tot}} = f_{\text{ch}} + f_{\text{intf}}$) is illustrated in Fig. 9c. We can tell that the term f_{ch} modifies the relative thermodynamic stability of the substance by shifting the free energy minima according to temperature changes. In contrast, γ grains at the same temperature do not show a difference in stability until the on-site temperature of one is changed.

The governing Eqs. for the coupled thermo-structural evolution are formulated as follows[28,29]

$$
\frac{\partial \rho}{\partial t} = \nabla \cdot \mathbf{M} \cdot \nabla \frac{\delta \mathcal{F}}{\delta \rho},
$$

(12a)

$$
\frac{\partial \phi_X^\gamma}{\partial t} = -L \frac{\delta \mathcal{F}}{\delta \phi_X^\gamma},
$$

(12b)

$$
c_{\text{r}}\left(\frac{\partial T}{\partial t} - \mathbf{v} \cdot \nabla T\right) = \nabla \cdot \mathbf{K} \cdot \nabla T + q_{\mathbf{v}},
$$

(12c)

where Eq. (12a) is the Cahn-Hilliard Eq. with the mobility tensor $\mathbf{M}$ specifically considering various mass transfer paths, incl. the mobilities for the mass transfer through the substance (ss), atmosphere (at), surface (sf) and grain boundary (gb). As elaborated in our former work[28], the localized melt flow driven by the local curvature is also modeled by one effective surface mobility $M_{\text{ml}}^{\text{eff}}$. $\mathbf{M}$ is then formulated as[33]

$$
\mathbf{M} = h_{\text{ss}}M_{\text{ss}}\mathbf{I} + h_{\text{at}}M_{\text{at}}\mathbf{I} + h_{\text{sf}}M_{\text{sf}}\mathbf{T}_{\text{sf}} + h_{\text{gb}}M_{\text{gb}}\mathbf{T}_{\text{gb}} + h_{\text{ml}}(T)M_{\text{ml}}^{\text{eff}}\mathbf{T}_{\text{sf}},
$$

(13)

with the 2nd-order identity tensor $\mathbf{I}$ and projection tensors $\mathbf{T}_{\text{sf}}$ and $\mathbf{T}_{\text{gb}}$ for surface and grain boundary, respectively[33,52]. The T-dependent values for M_{sf}, M_{gb}, M_{ss}, and $M_{\text{ml}}^{\text{eff}}$ are presented in Supplementary Fig. 5d. The interpolation functions on the surface and γ grain boundaries are defined as

$$
h_{\text{sf}} = 16\rho^2(1-\rho)^2, \qquad h_{\text{gb}} = 16\sum_{i\neq j}(\phi_i^\gamma \phi_j^\gamma)^2.
$$

Equation (12b) is the Allen-Cahn Eq. with the scalar mobility L, which is derived from the γ grain boundary mobility $G_{\gamma/\gamma}$ as[53,54]

$$
L = \frac{G_{\gamma/\gamma}\Gamma_{\gamma/\gamma}}{\underline{\kappa}_{\gamma/\gamma}},
$$

(14)

which is also presented in Supplementary Fig. 5d.

Equation (12c) is the heat transfer equation that considers the laser-induced thermal effect as a volumetric heat source $q_{\mathbf{v}}$.

$$
q_{\mathbf{v}}(\mathbf{r}, t) = Pp_{xy}[\mathbf{r}_O(\mathbf{v}, t)]\frac{\text{d}a}{\text{d}z},
$$

in which p_{xy} indicates the in-plane Gaussian distribution with a moving center $\mathbf{r}_O(\mathbf{v}, t)$. P is the beam power and $\mathbf{v}$ is the scan velocity with its magnitude $v = |\mathbf{v}|$ as the scan speed. The absorptivity profile function along depth $\text{d}a/\text{d}z$ is calculated based on refs. [28,55]. The phase-dependent thermal conductivity tensor is formulated in a form considering the continuity of the thermal flux along the normal/tangential direction of the surface[52,56], i.e.,

$$
\mathbf{K} = K_\perp \mathbf{N}_{\text{sf}} + K_\parallel \mathbf{T}_{\text{sf}}
$$

(15)

with

$$
K_\perp = h_{\text{ss}}K_{\text{ss}} + h_{\text{at}}K_{\text{at}}, \qquad K_\parallel = \frac{K_{\text{ss}}K_{\text{at}}}{h_{\text{ss}}K_{\text{at}} + h_{\text{at}}K_{\text{ss}}},
$$

where K_{ss} and K_{at} are the thermal conductivity of the substance and pore/atmosphere. $\mathbf{N}$ is the 2nd-order normal tensor of the surface[34,52]. Thermal resistance on the surface and γ/γ interface are disregarded, and will be presented in the upcoming works. While temperature-dependent K_{ss} takes the linear form in this work (Supplementary Fig. 5b), K_{at} specifically considers the radiation contribution via pore/atmosphere and is formulated as

$$
K_{\text{at}} = K_0 + 4FT^3\sigma_B\ell_{\text{rad}},
$$

(16)

where $K_0 \approx 0.06\,\text{W m}^{-1}\,\text{K}^{-1}$ is the thermal conductivity of the Argon gas, $F = 1/3$ is the Damköhler view factor[57], and $\sigma_B = 5.67 \times 10^{-8}\,\text{W m}^{-2}\,\text{K}^{-4}$ is the Stefan-Boltzmann constant. ℓ_{rad} is the effective radiation path between particles, which usually takes the average diameter of the powders[58].

As the boundary conditions (BC), no mass transfer is allowed on all the boundaries of the mesoscopic domain, which is achieved by setting Neumann BC on ρ as zero. The temperature at the bottom of the substrate mesh (z_{min}) is fixed at T_0 via Dirichlet BC on T. Heat transfer is allowed only via the pore/atmosphere, achieved by the combined BC of convection and radiation and masked by h_{at}), as illustrated in Supplementary Fig. 2d.

Mesoscopic thermo-elasto-plastic simulations

As elaborated in the subsection *Multiphysics-multiscale simulation scheme* and our former work[29], the subsequent thermo-elasto-plastic simulation was carried out for the calculation of the thermal stress and deformation of the mesostructures from the non-isothermal phase-field simulations of SLS processing. The transient temperature field and substance field ρ are imported into the quasi-static elasto-plastic model as the thermal load and the phase indicator for interpolating mechanical properties. Adopting small deformation and quasi-static assumptions, the mechanical equilibrium reads

$$
\nabla \cdot \boldsymbol{\sigma} = \mathbf{0},
$$

(17)

where $\boldsymbol{\sigma}$ is the 2nd-order stress tensor. The top boundary is set to be traction free, and the other boundaries adopt rigid support BCs,

which only restrict the displacement component in the normal direction of the boundary Supplementary Fig. 2e.

Taking the Voigt-Taylor interpolation scheme (VTS), where the total stress is interpolated according to the amount of the substance and pore/substance across the interface, i.e., $\boldsymbol{\sigma} = h_\gamma \boldsymbol{\sigma}^\gamma + h_{\gamma'} \boldsymbol{\sigma}^{\gamma'}$, while assuming identical strain among phases[59–61]. In this regard, the stress can be eventually formulated by the linear constitutive Eq.

$$\boldsymbol{\sigma} = \mathbf{C}(\rho, T) : (\boldsymbol{\varepsilon} - \boldsymbol{\varepsilon}_{th} - \boldsymbol{\varepsilon}_{pl} - \boldsymbol{\varepsilon}_{em}), \tag{18}$$

where $\boldsymbol{\varepsilon}_{th}$ is the thermal eigenstrain and $\boldsymbol{\varepsilon}_{pl}$ is the plastic strain. Notably, the magnetostrictive strain $\boldsymbol{\varepsilon}_{em}$ should be considered when the local temperature is below Curie temperature T_C due to the existence of spontaneous magnetization. This contribution, however, is assumed to be negligible compared to the developed plastic strain during the SLS and cooling stage and was tentatively dropped in this work. The 4th-order elastic tensor is interpolated from the substance one $\mathbf{C}_{ss}$ and the pores/atmosphere one $\mathbf{C}_{at}$, i.e.,

$$\mathbf{C}(\rho, T) = h_{ss}(\rho)\mathbf{C}_{ss}(T) + h_{at}(\rho)\mathbf{C}_{at}. \tag{19}$$

In this work, isotropic mechanical properties are considered. $\mathbf{C}_{ss}$ is calculated from the Young's modulus $E(T)$ and Poisson's ratio ν. In contrast, $\mathbf{C}_{at}$ is assigned with a sufficiently small value to guarantee the numerical convergence. The thermal eigenstrain $\boldsymbol{\varepsilon}_{th}$ is calculated using the interpolated coefficient of thermal expansion, i.e.,

$$\boldsymbol{\varepsilon}_{th} = a(\rho, T)[T - T_0]\mathbf{I}, \\ a(\rho, T) = h_{ss}(\rho)a_{ss}(T) + h_{at}(\rho)a_{at}, \tag{20}$$

where a_{ss} is obtained from temperature-dependent molar volume of the binary system V_m^{sys}, i.e.,

$$a = \frac{1}{3}\frac{1}{V_m^{sys}}\frac{\partial V_m^{sys}}{\partial T}. \tag{21}$$

Meanwhile, for plastic strain $\boldsymbol{\varepsilon}_{pl}$, the isotropic hardening model with the von Mises yield criterion is employed. The yield condition is determined as

$$f(\boldsymbol{\sigma}, p_e) = \sigma_e - (\sigma_y + Hp_e) \leq 0 \tag{22}$$

with

$$\sigma_e = \sqrt{\frac{3}{2}\mathbf{s} : \mathbf{s}}, \quad p_e = \int \sqrt{\frac{2}{3}, d\boldsymbol{\varepsilon}_{pl} : d\boldsymbol{\varepsilon}_{pl}},$$

where σ_e is the von Mises stress. $\mathbf{s}$ is the deviatoric stress, σ_y is the yield stress when no plastic strain is present. The isotropic plastic modulus H can be calculated from the isotropic hardening tangent modulus E_t and Young's modulus E as $H = EE_t/(E - E_t)$. These temperature-dependent mechanical properties are collectively presented in Supplementary Fig. 6. p_e is the accumulated plastic strain, which is integrated implicitly from the plastic strain increment $d\boldsymbol{\varepsilon}_{pl}$ obtained from the radial return method[62,63]. It is worth noting that the plastic strain is reset as zero once $T > T_M$ in emulating the effect of partial/full melting.

Nanoscopic chemical order-disorder (γ/γ') transition

Once the temperature drops below $T_{\gamma/\gamma'}$, the historical quantities (notably $T(t)$ and $\boldsymbol{\sigma}(t)$) will be sampled and imported to the nanoscopic domain for the subsequential γ/γ' simulations. Here we consider the nanoscopic (γ/γ') transition that occurs localized inside one γ grain, where ρ and only one ϕ_χ^γ are unity while other OPs are zero. This means the orientation information of the γ grain and the influences from the surface and γ/γ interface have been omitted on this scale. The growing γ' is also known to be orientation-coherent based on the experimental observations[18,19]. In this regard, the subscript χ, indicating the different grain orientations, is dropped in the following discussions. Magnetic

contribution f_{mag} is also dropped since the magnetic-field-free γ/γ' transition is scoped in this work. The profiles of ϕ^γ and $\phi^{\gamma'}$ across the γ/γ' interface are illustrated in Fig. 9b. Similarly, we take simplified notations in this subsection, such as $\phi = \phi^{\gamma'}$ and $X = X_{Ni}$ as the independent phase and concentration indicators, while $X_{Fe} = 1 - X$ and $\phi^\gamma = 1 - \phi$.

Due to the co-existence of both γ and γ' once the temperature is below $T_{\gamma/\gamma'} = 766$ K, the chemical free energy density should be formulated as

$$f_{ch}(T, \phi, \{X^\varphi\}) = h_\gamma(\phi)f_{ch}^\gamma(T, X^\gamma) + h_{\gamma'}(\phi)f_{ch}^{\gamma'}(T, X^{\gamma'}), \tag{23}$$

where h_γ and $h_{\gamma'}$ are monotonic interpolation functions and can adopt the polynomial formulation as

$$h_{\gamma'}(\phi) = \phi^3(10 - 15\phi + 6\phi^2), \quad h_\gamma(\phi) = 1 - \phi^3(10 - 15\phi + 6\phi^2).$$

Similarly the elastic contribution is formulated as[64,65]

$$f_{el}(T, \{\boldsymbol{\varepsilon}_{el}^\varphi\}) = h_\gamma(\phi)f_{el}^\gamma(T, \boldsymbol{\varepsilon}_{el}^\gamma) + h_{\gamma'}(\phi)f_{el}^{\gamma'}(T, \boldsymbol{\varepsilon}_{el}^{\gamma'}), \tag{24}$$

where

$$f_{el}^\varphi(T, \boldsymbol{\varepsilon}_{el}) = \frac{1}{2}\boldsymbol{\sigma}^\varphi : \boldsymbol{\varepsilon}_{el}^\varphi.$$

On top of the CALPHAD modeling of the free energy density of the chemical-disordered γ phase, the four-sublattice model is employed to describe the phase with chemical ordering. The model takes the element fractions $Y_i^{(s)}$ ($i =$ Fe or Ni indicating the chemical constituents, $s = 1, 2, 3, 4$ indicating the sublattice site, see inset of Fig. 9c) in each sublattice as the inner degree-of-freedoms, formulated as

$$f_{ch}^{\gamma'} = f_{ch}^\gamma + \{f_{4sl} - f_{4sl}(Y^{(s)} = X^\gamma)\}_{min} \tag{25}$$

with

$$f_{4sl}(T, Y_i^{(s)}) = \sum_{i,j,k,l} Y_i^{(1)}Y_j^{(2)}Y_k^{(3)}Y_l^{(4)}f_{ijkl}^{FCC} + \frac{\mathcal{R}T}{4V_m^{sys}}\sum_{s,i}Y_i^{(s)}\ln Y_i^{(s)} \\ + \sum_s \left[Y_i^{(s)}\left(1 - Y_i^{(s)}\right)\sum_{j,k,l}Y_j^{(u)}Y_k^{(v)}Y_l^{(w)}\frac{L_{(s)ijkl}^{FCC}}{V_m^{sys}}\right], \tag{26}$$

where f_{ijkl}^{FCC} are the free energies of the stoichiometric compounds with only one constituent ($i, j, k, l =$ Ni or Fe) occupied on each site[47]. $L_{(s)ijkl}^{FCC}$ is the interaction parameter, corresponding to the mixing of constituents on the s-th site while others ($u, v, w \neq s$) are with the fractions $Y_j^{(u)}$, $Y_k^{(v)}$ and $Y_l^{(w)}$. Note that the constraints $\sum_s Y_i^{(s)} = X_i$ and $Y_{Ni}^{(s)} + Y_{Fe}^{(s)} = 1$ should be applied to guarantee the conservation of atom. It is also worth noting that due to the thermodynamic equivalence of four sublattice sites, the equivalence of f_{ijkl}^{FCC} and $L_{(s)ijkl}^{FCC}$ regarding the combination of sublattice constituents must be considered, as explicitly explained in ref. [47]. All the thermodynamic parameters for the CALPHAD are obtained from ref. [47]. In Supplementary Fig. 8. we present the calculated f_{ch}^γ and $f_{ch}^{\gamma'}$ from the $T_{\gamma/\gamma'}$ to the pre-heating temperature $T_0 = 600$ K with the varying equilibrium concentration of X_e^γ and $X_e^{\gamma'}$, the site element fraction $Y^{(s)}$, and the calculated phase fraction Ψ_γ and $\Psi_{\gamma'}$ under the equilibrium.

On the other hand, since there is only the γ/γ' coherent interface, the non-isothermal local and gradient free energy density are then formulated in the typical double-well fashion, i.e.,

$$f_{loc}(T, \phi) = 12\underline{W}_{\gamma/\gamma'}(T)\phi^2(1 - \phi)^2, \quad f_{grad}(T, \nabla\phi) = \frac{1}{2}\underline{\kappa}_{\gamma/\gamma'}(T)|\nabla\phi|^2 \tag{27}$$

with

$$\underline{W}_{\gamma/\gamma'}(T) = W_{\gamma/\gamma'}\tau_{\gamma/\gamma'}(T), \quad \underline{\kappa}_\phi(T) = \kappa_{\gamma/\gamma'}\tau_{\gamma/\gamma'}(T),$$

adapting the same non-isothermal form as the one used in the SLS simulations with the dimensionless temperature tendency $\tau_{\gamma/\gamma'}(T)$. The temperature-independent parameters $W_{\gamma/\gamma'}$ and $\kappa_{\gamma/\gamma'}$

are obtained from the interface energy $\Gamma_{\gamma/\gamma'}$ and diffuse-interface width $\ell_{\gamma/\gamma'}$, i.e.,

$$\Gamma_{\gamma/\gamma'}(T) = \frac{\sqrt{6}}{3} \tau_{\gamma/\gamma'}(T) \sqrt{W_{\gamma/\gamma'} \kappa_{\gamma/\gamma'}}, \qquad \ell_{\gamma/\gamma'} \approx \frac{\sqrt{6}}{3} \sqrt{\frac{\kappa_{\gamma/\gamma'}}{W_{\gamma/\gamma'}}}, \qquad (28)$$

noting that the relation of $\ell_{\gamma/\gamma'}$ here corresponds to the case when adjusting parameter as two in Eq. (53) of the ref. [66]. In this work, we tentatively take $\tau_{\gamma/\gamma'}$ as one and estimate $\Gamma_{\gamma/\gamma'} = 0.025\,\mathrm{J\,m}^{-2}$, which is a commonly estimated value for the coherent interfaces and lies between the experimental range from 0.008 to 0.080 J m^{-2} for the Ni-base alloys[67]. The diffuse-interface width $\ell_{\gamma/\gamma'}$ is given as 5 nm. The total free energy at stress-free condition ($f_{tot} = f_{ch} + f_{intf}$) is illustrated in Fig. 9d, where the free energy density path obeying the mixing rule is also illustrated across the γ/γ' interface between two equilibrium phases (i.e., with X_e^γ and $X_e^{\gamma'}$).

The governing Eqs. of the nanoscopic γ/γ' transition is formulated as follows[64,66]

$$X = h_\gamma X^\gamma + h_{\gamma'} X^{\gamma'}, \qquad (29a)$$

$$\frac{df_{ch}^\gamma}{dX^\gamma} = \frac{df_{ch}^{\gamma'}}{dX^{\gamma'}}, \qquad (29b)$$

$$\frac{\partial X}{\partial t} = \nabla \cdot M_X \nabla \frac{\delta \mathcal{F}}{\delta X}, \qquad (29c)$$

$$\frac{\partial \phi}{\partial t} = -M_\phi \frac{\delta \mathcal{F}}{\delta \phi}, \qquad (29d)$$

$$\nabla \cdot \boldsymbol{\sigma} = \mathbf{0}. \qquad (29e)$$

Notably, Eq. (29a) embodies the mixing rule of the local Ni concentration X from the phase ones X^γ and $X^{\gamma'}$, considering the γ/γ' interface as a two-phase mixture with ϕ as the local phase fraction. This detaches the chemical and local contributions to the interface energy to allow rescalability of the diffuse-interface width. Equation (29b) is the constraint to the phase concentration

X^γ and $X^{\gamma'}$ to obtain the maximum driving force for the interface migration, as briefly elaborated in Supplementary Fig. 9. In return, the drag effect might be eliminated along with the vanishing of the driving force for trans-interface diffusion[68–71], which should be specifically evaluated and discussed for the γ/γ' transition in the Fe-Ni system. The diffusive mobility M_X here is directly formulated by the atom mobilities M_{Fe} and M_{Ni} in the FCC lattice considering the inter-diffusion phenomena[72], i.e.,

$$M_X(X, T) = V_m^{sys} X(1-X)[(1-X)M_{Fe}(T) + X M_{Ni}(T)], \qquad (30)$$

and the interface migration mobility M_ϕ is derived by considering the thin-interface limit of the model and the interface migration rate that was originally derived by Turnbull[54,69], i.e.,

$$M_\phi(T) = \frac{2}{3} \frac{V_m^{sys} \Phi_{\gamma'/\gamma}}{\mathrm{Ch}|\mathbf{b}|^2} \left[(1 - X_{\gamma'/\gamma}) M_{Fe}(T) + X_{\gamma'/\gamma} M_{Ni}(T) \right], \qquad (31)$$

where the dimensionless Cahn number $\mathrm{Ch} = \ell_{\gamma/\gamma'} / \hat{\ell}_{\gamma/\gamma'}$, characterizing the degree of the rescaling of the diffuse-interface width $\ell_{\gamma/\gamma'}$ from the realistic interface width $\hat{\ell}_{\gamma/\gamma'}$, which is estimated as $\hat{\ell}_{\gamma/\gamma'} = 5\bar{a}$ with $\bar{a}$ the average lattice parameter of the γ and γ' phases based on the experimental observation[73]. Length of the burgers vector is also calculated from $\bar{a}$ by $|\mathbf{b}| = \bar{a}/\sqrt{2}$. $\Phi_{\gamma'/\gamma}$ is a newly defined thermodynamic factor with the estimated interface concentration $X_{\gamma'/\gamma}$ as

$$\Phi_{\gamma'/\gamma} = X_{\gamma'/\gamma}(1 - X_{\gamma'/\gamma}) \frac{V_m^{sys}}{\mathcal{R}T} \frac{\partial^2 f_{ch}}{\partial X^2}\bigg|_{\gamma'/\gamma},$$

$$X_{\gamma'/\gamma} = \frac{X_e^\gamma / A_m^\gamma + X_e^{\gamma'} / A_m^{\gamma'}}{1/A_m^\gamma + 1/A_m^{\gamma'}}$$

with the equilibrium concentrations X_e^γ and $X_e^{\gamma'}$ as well as the molar area of the phases A_m^γ and $A_m^{\gamma'}$. The detailed derivations are shown in the Supplementary Note 2. The temperature-dependent atom mobility $M_{Ni}(T)$ and $M_{Fe}(T)$ are obtained from the mobility database MOBFE3 from the commercial software Thermo-Calc®[51].

In this work, it should be highlighted that a temperature-dependent dimensionless calibration factor $\omega(T)$ is additionally associated with the atom mobilities, which is utilized to be
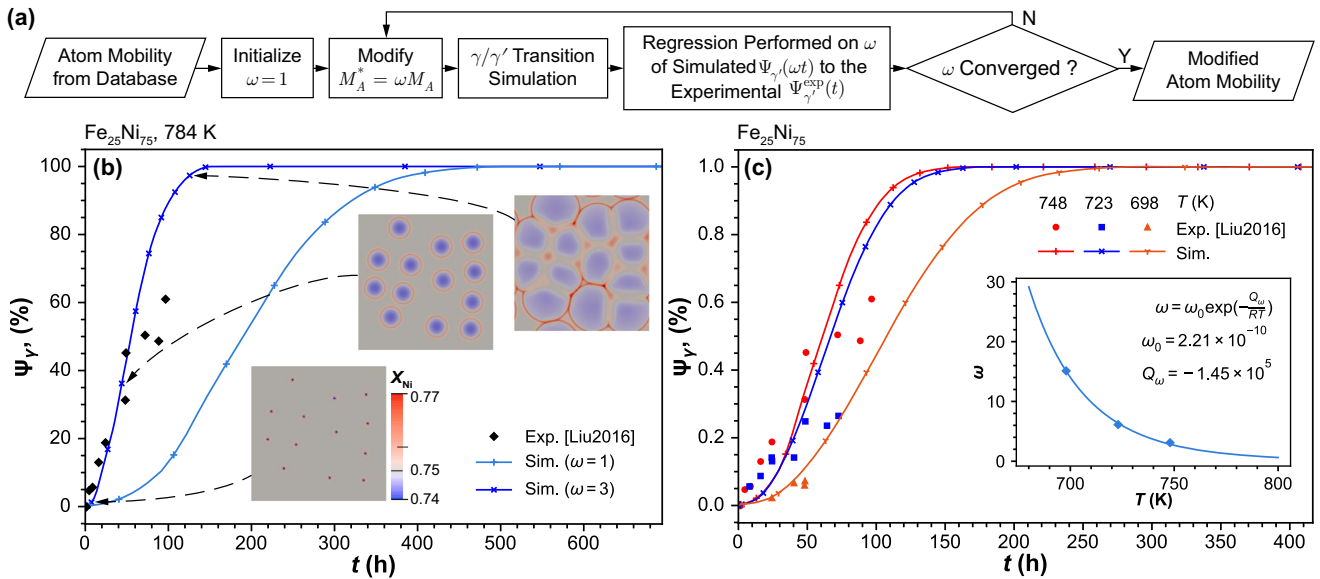

Fig. 10 Calibration of atom mobility for nanoscopic γ/γ' transition. a Workflow for the calibration of the atom mobility by iteratively performing regression on the factor ω from $\Psi_{\gamma'}(\omega t)$ w.r.t. the experimental measured $\Psi_{\gamma'}^{exp}(t)$. The ω that has a difference of less than 0.5% to the last interaction is identified as the converged value for the current temperature. **b** Simulated $\Psi_{\gamma'}(t)$ at 784 K with the mobilities before ($\omega = 1$) and after ($\omega = 3$) calibration cf. $\Psi_{\gamma'}^{exp}(t)$ from[30], with the nanostructures denoted at corresponding time point. **c** Simulated $\Psi_{\gamma'}(t)$ vs $\Psi_{\gamma'}^{exp}(t)$ at different temperatures. Inset: Regression of calibrated $\omega(T)$ to the Arrhenius Eq., which presents consistency. Notice that both experiments and simulations are performed with composition Fe$_{25}$Ni$_{75}$.

calibrated from the experimentally measured γ/γ' transition with respect to time at various temperatures. The calibrated atom mobility is then shown as (noting $A = $ Fe, Ni)

$$M_A^*(T) = \omega(T)M_A(T). \tag{32}$$

Based on the Arrhenius relation on temperature for $M_A(T)$ and $M_A^*(T)$[72,74], this $\omega(T)$ is postulated to follow the Arrhenius relation as well, i.e., $\omega(T) = \omega_0 \exp(-Q_\omega/\mathcal{R}T)$ with the pre-factor ω_0 and the activation energy Q_ω. We implemented a simple calibration algorithm by iteratively performing the regression on ω as the time scaling factor to the simulated transient volume fraction of γ' phase, i.e., $\Psi_{\gamma'}(\omega t)$ with respect to the experimental measurements obtained from[30], as shown in Fig. 10a. The IC of the γ' nuclei was generated using Poisson disk sampling[38] with the prescribed minimum nuclei distance according to the observation shown in Fig. 1b. The calibrated $\omega(T)$ indeed shows consistency to the Arrhenius relation, confirming our postulate.

As for momentum balance in Eq. (29e), we have to explicitly consider both long-range (morphology and morphology-induced chronological-spatial thermal inhomogeneity) and short-range factors (misfit-induced fluctuation) factors of the mechanical response on the current scale. In that sense, the stress should be considered in the following form

$$\boldsymbol{\sigma} = \boldsymbol{\sigma}_{\mathrm{ms}} + \tilde{\boldsymbol{\sigma}}, \tag{33}$$

where $\boldsymbol{\sigma}_{\mathrm{ms}}$ comes from the mesoscale and $\tilde{\boldsymbol{\sigma}}$ is incited due to the misfit of growing γ' phase. Assuming the stiffness tensor $\mathbf{C}_{\mathrm{ss}}$ has no differences between the two phases, we then take a uniform elastic strain that attributes to the mesoscopic stress, i.e., $\boldsymbol{\sigma}_{\mathrm{ms}} = \mathbf{C}_{\mathrm{ss}} : \boldsymbol{\varepsilon}_{\mathrm{el}}^{\mathrm{ms}}$. The constitutive relation can then be represented as

$$\begin{aligned}
\boldsymbol{\sigma} &= \mathbf{C}_{\mathrm{ss}} : \boldsymbol{\varepsilon}_{\mathrm{el}} + \boldsymbol{\sigma}_{\mathrm{ms}} \\
&= \mathbf{C}_{\mathrm{ss}} : \left[\left(\boldsymbol{\varepsilon} - \boldsymbol{\varepsilon}_{\mathrm{em}} - h_{\gamma'}\varepsilon_{\mathrm{mis}}^{\gamma'}\mathbf{I} \right) + \boldsymbol{\varepsilon}_{\mathrm{el}}^{\mathrm{ms}} \right],
\end{aligned} \tag{34}$$

where $\boldsymbol{\varepsilon}$ is the total strain calculated on the nanoscopic domain, $\boldsymbol{\varepsilon}_{\mathrm{em}}$ is the magnetostrictive strain, and $\varepsilon_{\mathrm{mis}}^{\gamma'}$ is the misfit strain induced by growing γ' phase. $\varepsilon_{\mathrm{mis}}^{\gamma'}$ is the relative difference between lattice parameters of the γ and γ' phases, i.e., $\varepsilon_{\mathrm{mis}}^{\gamma'} = (a_{\gamma'} - a_\gamma)/a_\gamma$ with a_γ and $a_{\gamma'}$ obtained from the temperature-dependent molar volume V_m^γ and $V_m^{\gamma'}$, respectively. This is presented in Supplementary Fig. 7b. At $T_0 = 600$ K, this $\varepsilon_{\mathrm{mis}}^{\gamma'} = -1.32 \times 10^{-3}$. It is worth noting that $\boldsymbol{\varepsilon}_{\mathrm{em}}$ incited by spontaneous magnetization is also assumed to have negligible effects on γ/γ' transition compared to $\varepsilon_{\mathrm{mis}}^{\gamma'}$ and $\boldsymbol{\varepsilon}_{\mathrm{el}}^{\mathrm{ms}}$, which is due to the relatively small magnetostriction constants λ_{100} and λ_{111} in the chemical composition range, i.e., $X_{\mathrm{Ni}} = 0.781 \sim 0.785$, leading to $\boldsymbol{\varepsilon}_{\mathrm{em}}$ on the order of 10^{-6} compared to $\varepsilon_{\mathrm{mis}}^{\gamma'}$ and $\boldsymbol{\varepsilon}_{\mathrm{el}}^{\mathrm{ms}}$ on the order of $10^{-4} \sim 10^{-3}$. Alongside with $\boldsymbol{\varepsilon}_{\mathrm{el}}^{\mathrm{ms}}$ as an eigenstrain, the periodic displacement BC are applied to the nanoscopic domain, as shown in Supplementary Fig. 2.

Micromagnetic hysteresis simulations

Below the Curie temperature, the magnetization of most ferromagnetic materials saturates with constant magnitude (M_s). Therefore in micromagnetics, it is important to have a normalized magnetization vector that is position-dependent, i.e., $\mathbf{m}$. This vector field can be physically interpreted as the mean field of the local atom magnetic moments, but yet sufficiently small in scale to resolve the magnetization transition across the domain wall. However, variation of $\mathbf{m}(\mathbf{r})$ across the γ/γ' interface is tentatively disregarded as an ideal exchange coupling between two phases. Magnetic properties in the ferromagnetic γ phase are also tentatively assumed to be identical to the ferromagnetic γ' at the same Ni-concentration due to the lack of experimental/theoretical investigations on the magnetic properties of individual phases. In other words, only the Ni-concentration dependency of magnetic parameters is explicitly considered in this work, while

the exchange constant A_{ex} takes constant as 13 pJ/m[75]. In that sense, superscript φ, indicating the phase differences, is dropped in the following explanation. We let the orientation $\mathbf{u}$ of the nanoscopic subdomain align on the z-direction (BD), and the magnetic free energy density is eventually formulated as

$$f_{\mathrm{mag}} = f_{\mathrm{ex}} + f_{\mathrm{ani}} + f_{\mathrm{ms}} + f_{\mathrm{zm}} + f_{\mathrm{em}} \tag{35}$$

with

$$\begin{aligned}
f_{\mathrm{ex}}(\nabla\mathbf{m}) &= A_{\mathrm{ex}}\|\nabla\mathbf{m}\|^2, \\
f_{\mathrm{ani}}(\mathbf{m}) &= -K_u(\mathbf{u} \cdot \mathbf{m})^2, \\
f_{\mathrm{ms}}(\mathbf{m}) &= -\tfrac{1}{2}\mu_0 M_s \mathbf{m} \cdot \mathbf{H}_{\mathrm{dm}}, \\
f_{\mathrm{zm}}(\mathbf{m}, \mathbf{H}_{\mathrm{ext}}) &= -\mu_0 M_s \mathbf{m} \cdot \mathbf{H}_{\mathrm{ext}}, \\
f_{\mathrm{em}}(\mathbf{m}, \boldsymbol{\sigma}) &= -\boldsymbol{\sigma} : \boldsymbol{\varepsilon}_{\mathrm{em}},
\end{aligned}$$

and the magnetostrictive strain $\boldsymbol{\varepsilon}_{\mathrm{em}}$ on the cubic basis as follows[39,40]

$$\boldsymbol{\varepsilon}_{\mathrm{em}} = \frac{3}{2}\begin{bmatrix} \lambda_{100}\left(m_x^2 - \tfrac{1}{3}\right) & \lambda_{111}m_x m_y & \lambda_{111}m_x m_z \\ & \lambda_{100}\left(m_y^2 - \tfrac{1}{3}\right) & \lambda_{111}m_y m_z \\ \text{symm.} & & \lambda_{100}\left(m_z^2 - \tfrac{1}{3}\right) \end{bmatrix}.$$

Here, f_{ex} is the exchange contribution, recapitulating the parallel-aligning tendency among neighboring magnetic moments due to the Heisenberg exchange interaction. The norm $\|\nabla\mathbf{m}\|$ here represents $\sum_j |\nabla m_j|^2$ with $j = x, y, z$ and $\mathbf{m} = [m_x, m_y, m_z]$. f_{ani} represents the contribution due to the magneto-crystalline anisotropy. It provides the energetically preferred orientation to local magnetizations with respect to the crystalline orientation $\mathbf{u}$ according to the sign of the K_u. f_{ani} represents the contribution due to the magneto-crystalline anisotropy. It provides the energetically preferred orientation to local magnetizations with respect to the crystalline orientation $\mathbf{u}$, concerning the sign of the K_u. Defining an orientation angle by $\vartheta = \arccos\mathbf{u} \cdot \mathbf{m}$, the case when $K_u > 0$ leads two energetic minima at $\vartheta = 0$ and π, that is when the magnetization lies along the positive or negative $\mathbf{u}$ direction with no preferential orientation, i.e., the easy-axis anisotropy. When $K_u < 0$, the energy is minimized for $\vartheta = \pi/2$, meaning that any direction in the plane perpendicular to $\mathbf{u}$ is thermodynamically preferred, i.e., the easy-plane anisotropy[31], as shown in Fig. 9e, f. As the resulting X_{Ni} varies from 0.781 to 0.810 as presented in Fig. 5, local K_u always takes the negative value in this work. The magnetostatic term f_{ms} counts the energy of each local magnetization under the demagnetizing field created by the surrounding magnetization. The Zeeman term f_{zm} counts the energy of each local magnetization under an extrinsic magnetic field $\mathbf{H}_{\mathrm{ext}}$. f_{em} is the contribution due to the magneto-elastic coupling effects.

Evolution of the magnetization configuration $\mathbf{m}(\mathbf{r})$ under a cycling $\mathbf{H}_{\mathrm{ext}}$ was generally described by the Landau-Lifshitz-Gilbert Eq., which is mathematically formulated as

$$\frac{\partial\mathbf{m}}{\partial t} = \frac{\gamma_{\mathrm{mg}}}{1 + a_d^2}\frac{1}{\mu_0 M_s}\left[\mathbf{m} \times \frac{\delta\mathcal{F}}{\delta\mathbf{m}} + a_d\mathbf{m} \times \left(\mathbf{m} \times \frac{\delta\mathcal{F}}{\delta\mathbf{m}}\right)\right] \tag{36}$$

with the vacuum permeability μ_0, the gyromagnetic ratio γ_{mg} and the damping coefficient a_d[76]. However, due to the incomparable time scale of LLG-described magnetization dynamics (around nanoseconds) with respect to the one of hysteresis measurement (around seconds), constrained optimization of the free energy functional $\mathcal{F}$ has been widely employed as a computationally efficient alternative to the time-dependent calculation in evaluating the hysteresis behavior of permanent magnets[77–79]. Based on the steepest conjugate gradient (SCG) method, the iteration scheme is derived as

$$\frac{\mathbf{m}^{(i+1)} - \mathbf{m}^{(i)}}{\Delta^{(i)}} = \mathbf{m}^{(i)} \times \frac{1}{\mu_0 M_s}\left[\mathbf{m}^{(i)} \times \frac{\delta\mathcal{F}}{\delta\mathbf{m}^{(i)}}\right],$$
$$\text{subject to} \quad |\mathbf{m}| = 1 \tag{37}$$

with the iteration step size $\Delta^{(i)}$ and the magnetization configuration $\mathbf{m}^{(i)}$ of the step i. The iteration scheme in Eq. (37) is in accordance with the sole damping term of the LLG equation Eq. (36)[77,79]. This also means that the magnetic hysteresis is evaluated under the quasi-static condition. The simulation domains with the FD grids have the same construction as the FE meshes used in the γ/γ' transition simulations to ease the quantity mapping in-between. Periodic BC was applied on the boundaries perpendicular to z-direction by macro geometry approach[80], while Neumann BC was applied on the other boundaries[35].

It is also worth noting that the magneto-elastic coupling constants B_1 and B_2, calculated by $\lambda_{100} = -2B_1/3(C_{11} - C_{12})$ and $\lambda_{111} = -B_2/3C_{44}$[39,81] are implemented in the package MuMax^3. The elastic strain field that attributes to the residual stress, i.e., $\boldsymbol{\sigma} = \mathbf{C}_{ss}:\boldsymbol{\varepsilon}_{el}$, are mapped from the nanoscopic γ/γ' transition results.

Implementations and parallel computations

Both non-isothermal phase-field and thermo-elasto-plastic models are numerically implemented by the finite element method within the program NIsoS[28,33], developed by the authors based on the MOOSE framework (Idaho National Laboratory, ID, USA)[82,83]. The 8-node hexahedron Lagrangian elements were chosen to mesh the geometry. A transient solver with preconditioned Jacobian-Free Newton-Krylov method (PJFNK) was employed in both models. Each simulation was executed with 96 AVX512 processors and 3.6 GByte RAM per processor based on MPI parallelization. The associated CALPHAD calculations were conducted by open-sourced package PyCALPHAD[84], and the thermodynamic data intercommunication was carried out by customized Python and C ++ codes. The DEM-based powder bed generation is conducted by the open-sourced package YADE[28,85].

For SLS simulations, the Cahn-Hilliard Eq. in Eq. (12a) was solved in a split way. The constraint of the order parameters was enforced by the penalty method. To reduce computation costs, h-adaptive meshing and time-stepping schemes are used. The initial structured mesh is presented in Supplementary Fig. 2a. The additive Schwarz method (ASM) preconditioner with the incomplete LU-decomposition sub-preconditioner was also employed for parallel computation of the vast linear system, seeking the balance between memory consumption per core and computation speed[86]. The backward Euler method was employed for the time differentials, and the constraint of the order parameters was fulfilled using the penalty method. Due to the usage of h-adaptive meshes, the computational costs vary from case to case. The peak DOF number is on order 10,000,000 for both the nonlinear system and the auxiliary system. The peak computational consumption is on the order of 10,000 core-hour. More details about the FEM implementation are shown in the supplementary information of ref. [28].

For thermo-elasto-plastic simulations, a static structured mesh was utilized Supplementary Fig. 2b to avoid the hanging nodes generated from the h-adaptive meshing scheme. In that sense, the transient fields T and ρ of each calculation step were uni-directionally mapped from the non-isothermal phase-field results (with h-adaptive meshes) into the static meshes. This is achieved by the MOOSE-embedded `SolutionUserObject` class and associated functions. The parallel algebraic multigrid precondi-tioner BoomerAMG was utilized with the Eisenstat-Walker (EW) method to determine linear system convergence. It is worth noting that a vibrating residual of non-linear iterations would show without employing the EW method for this work. The DOF number of each simulation is on the order of 1,000,000 for the nonlinear system and 10,000,000 for the auxiliary system. The computational consumption is on the order of 1,000 CPU core-hour.

For γ/γ' transition simulations, a static uniform mesh was utilized Supplementary Fig. 2c. 2nd backward Euler method was employed. The additive Schwarz method (ASM) preconditioner

with the complete LU-decomposition sub-preconditioner was also employed for parallel computation. The simulations were per-formed in a high-throughput fashion with 100 ~ 1000 transition simulations as a batch for one set of processing parameters. The DOF number of each simulation is on the order of 1,000,000 for the nonlinear system and 10,000,000 for the auxiliary system. The computational consumption of each simulation is 500 CPU core-hour by average.

The micromagnetic simulations were carried out by the FDM-based steepest conjugate gradient (SCG) solver performing Eq. (37) in the open-sourced package MuMax^3[35] with numerical details elaborated in ref. [77]. The high-throughput GPU-parallel computations were performed with 100 ~ 1000 micromagnetic simulations as a batch, each simulation has the DOF on the order of 100,000 for calculating the magnetization configuration, while the demagnetization field $\mathbf{H}_{dm}$ obtained via magnetostatic convolution of the magnetization rather than introducing extra DOF.

DATA AVAILABILITY
The authors declare that the data supporting the findings of this study are available within the paper. The temperature-dependent parameters, thermodynamic database, simulation results, supplementary data and utilities are cured in the online dataset (https://doi.org/10.5281/zenodo.7767663).

CODE AVAILABILITY
Source codes of MOOSE-based application NIsoS and related utilities are available and can be accessed via the online repository bitbucket.org/mfm_tuda/nisos.git.

REFERENCES

1. Fert, A. Nobel lecture: origin, development, and future of spintronics. *Rev. Mod. Phys.* **80**, 1517 (2008).
2. Silveyra, J. M., Ferrara, E., Huber, D. L. & Monson, T. C. Soft magnetic materials for a sustainable and electrified world. *Science* **362**, eaao0195 (2018).
3. Liu, Z., Li, S., Wang, F., Li, M. & Ni, Y. Hierarchically porous feni 3@ feni layered double hydroxide nanostructures: one-step fast electrodeposition and highly efficient electrocatalytic performances for overall water splitting. *Dalton Trans.* **50**, 6306–6314 (2021).
4. Hirano, N. et al. Feasibility study of high-efficiency cooling of high-temperature superconducting coils by magnetic refrigeration. *IEEE Trans. Appl. Supercond.* **31**, 1–4 (2021).
5. Zhang, B., Fenineche, N.-E., Zhu, L., Liao, H. & Coddet, C. Studies of magnetic properties of permalloy (fe-30% ni) prepared by slm technology. *J. Magn. Magn. Mater.* **324**, 495–500 (2012).
6. Mazeeva, A. et al. Magnetic properties of fe–ni permalloy produced by selective laser melting. *J. Alloys Compd.* **814**, 152315 (2020).
7. Mikler, C. et al. Tuning the phase stability and magnetic properties of laser additively processed fe-30at% ni soft magnetic alloys. *Mater. Lett.* **199**, 88–92 (2017).
8. Schönrath, H. et al. Additive manufacturing of soft magnetic permalloy from fe and ni powders: control of magnetic anisotropy. *J. Magn. Magn. Mater.* **478**, 274–278 (2019).
9. Kim, E. S. et al. Mechanical and magnetic properties of soft magnetic fe-ni per-malloy produced by directed energy deposition processes. *J. Mater. Sci.* **57**, 17967–17983 (2022).
10. Kim, E. S., Haftlang, F., Ahn, S. Y., Gu, G. H. & Kim, H. S. Effects of processing parameters and heat treatment on the microstructure and magnetic properties of the in-situ synthesized fe-ni permalloy produced using direct energy deposi-tion. *J. Alloys Compd.* **907**, 164415 (2022).
11. Zou, J. et al. Controlling the grain orientation during laser powder bed fusion to tailor the magnetic characteristics in a ni-fe based soft magnet. *Acta Mater.* **158**, 230–238 (2018).
12. Baco-Carles, V., Baylac, V., Pasquet, I., Plissonneau, B. & Tailhades, P. Soft chemistry synthesis and laser powder bed fusion processing of fe–ni alloy based powders: a

route for the manufacturing of porous multiphase fe–ni alloy parts. *Powder Technol.* **399**, 117200 (2022).

13. Bozorth, R. The permalloy problem. *Rev. Mod. Phys.* **25**, 42 (1953).

14. Reuter, K., Williams, D. B. & Goldstein, J. Ordering in the fe- ni system under electron irradiation. *Metall. Trans. A* **20**, 711–718 (1989).

15. Van deen, J. & Van Der Woude, F. Phase diagram of the order-disorder transition in ni3fe. *Acta Metall.* **29**, 1255–1262 (1981).

16. Ohnuma, I., Shimenouchi, S., Omori, T., Ishida, K. & Kainuma, R. Experimental determination and thermodynamic evaluation of low-temperature phase equilibria in the fe–ni binary system. *Calphad* **67**, 101677 (2019).

17. Wakelin, R. & Yates, E. A study of the order-disorder transformation in iron-nickel alloys in the region feni3. *Proc. Phys. Soc. B* **66**, 221 (1953).

18. Ustinovshchikov, Y. I., Shabanova, I. & Lomova, N. Microstructures responsible for the invar and permalloy effects in fe-ni alloys. *Russ. Metall. (Met.)* **2015**, 389–394 (2015).

19. Ustinovshikov, Y. & Shabanova, I. A study of microstructures responsible for the emergence of the invar and permalloy effects in fe-ni alloys. *J. Alloys Compd.* **578**, 292–296 (2013).

20. Zhang, B., Fenineche, N.-E., Liao, H. & Coddet, C. Magnetic properties of in-situ synthesized feni3 by selective laser melting fe-80% ni powders. *J. Magn. Magn. Mater.* **336**, 49–54 (2013).

21. Mohamed, A. E.-M. A., Zou, J., Sheridan, R. S., Bongs, K. & Attallah, M. M. Magnetic shielding promotion via the control of magnetic anisotropy and thermal post processing in laser powder bed fusion processed nifemo-based soft magnet. *Addit. Manuf.* **32**, 101079 (2020).

22. Yi, M., Xu, B.-X. & Gutfleisch, O. Computational study on microstructure evolution and magnetic property of laser additively manufactured magnetic materials. *Comput. Mech.* **64**, 917–935 (2019).

23. Renuka Balakrishna, A. & James, R. D. A solution to the permalloy problem—a micromagnetic analysis with magnetostriction. *Appl. Phys. Lett.* **118**, 212404 (2021).

24. Renuka Balakrishna, A. & James, R. D. Design of soft magnetic materials. *npj Comput. Mater.* **8**, 1–10 (2022).

25. Mercelis, P. & Kruth, J. Residual stresses in selective laser sintering and selective laser melting. *Rapid Prototyp. J.* **12**, 254–265 (2006).

26. Simson, T., Emmel, A., Dwars, A. & Böhm, J. Residual stress measurements on aisi 316l samples manufactured by selective laser melting. *Addit. Manuf.* **17**, 183–189 (2017).

27. Takezawa, A., Guo, H., Kobayashi, R., Chen, Q. & To, A. C. Simultaneous optimization of hatching orientations and lattice density distribution for residual warpage reduction in laser powder bed fusion considering layerwise residual stress stacking. *Addit. Manuf.* **60**, 103194 (2022).

28. Yang, Y., Ragnvaldsen, O., Bai, Y., Yi, M. & Xu, B.-X. 3d non-isothermal phase-field simulation of microstructure evolution during selective laser sintering. *npj Comput. Mater.* **5**, 1–12 (2019).

29. Zhou, X. et al. 3d-multilayer simulation of microstructure and mechanical properties of porous materials by selective sintering. *GAMM-Mitteilungen* **44**, e202100017 (2021).

30. Liu, J. et al. Kinetics of order-disorder transformation of l12 feni3 in the fe-ni system. *J. Alloys Compd.* **689**, 593–598 (2016).

31. Kronmuller, H., Kronmüller, H. et al. *Micromagnetism and the microstructure of ferromagnetic solids* (Cambridge University Press, 2003).

32. Armero, F. & Simo, J. A new unconditionally stable fractional step method for non-linear coupled thermomechanical problems. *Int. J. Numer. Methods Eng.* **35**, 737–766 (1992).

33. Yang, Y., Oyedeji, T. D., Kühn, P. & Xu, B.-X. Investigation on temperature-gradient-driven effects in unconventional sintering via non-isothermal phase-field simulation. *Scr. Mater.* **186**, 152–157 (2020).

34. Oyedeji, T. D., Yang, Y., Egger, H. & Xu, B. X. Variational quantitative phase-field modeling of non-isothermal sintering process. *arXiv preprint arXiv:2209.14913.* https://doi.org/10.48550/arXiv.2209.14913 (2022).

35. Vansteenkiste, A. et al. The design and verification of mumax3. *AIP Adv.* **4**, 107133 (2014).

36. Koepf, J. A., Gotterbarm, M. R., Markl, M. & Körner, C. 3d multi-layer grain structure simulation of powder bed fusion additive manufacturing. *Acta Materialia* **152**, 119–126 (2018).

37. Shi, R. et al. Microstructural control in metal laser powder bed fusion additive manufacturing using laser beam shaping strategy. *Acta Materialia* **184**, 284–305 (2020).

38. Bridson, R. Fast poisson disk sampling in arbitrary dimensions. *SIGGRAPH Sketches* **10**, 1 (2007).

39. Kittel, C. Physical theory of ferromagnetic domains. *Rev. Mod. Phys.* **21**, 541 (1949).

40. O'handley, R. C. *Modern magnetic materials: principles and applications* (Wiley, 2000).

41. Yang, Y. et al. Validated dimensionless scaling law for melt pool width in laser powder bed fusion. *J. Mater. Process. Technol.* **299**, 117316 (2022).

42. Körner, C., Attar, E. & Heinl, P. Mesoscopic simulation of selective beam melting processes. *J. Mater. Process. Technol.* **211**, 978–987 (2011).

43. Gu, H. et al. Multi-physics modelling of molten pool development and track formation in multi-track, multi-layer and multi-material selective laser melting. *Int. J. Heat Mass Transf.* **151**, 119458 (2020).

44. Gu, D. & Shen, Y. Balling phenomena in direct laser sintering of stainless steel powder: metallurgical mechanisms and control methods. *Mater. & Des.* **30**, 2903–2910 (2009).

45. Petrila, I. & Stancu, A. Hysteresis characteristics of an analytical vector hysteron. *Physica B: Condensed Matter* **406**, 906–910 (2011).

46. Steinbach, I. Phase-field models in materials science. *Model. Simul. Mater. Sci. Eng.* **17**, 073001 (2009).

47. Cacciamani, G., Dinsdale, A., Palumbo, M. & Pasturel, A. The fe-ni system: thermodynamic modelling assisted by atomistic calculations. *Intermetallics* **18**, 1148–1162 (2010).

48. Redlich, O. & Kister, A. Algebraic representation of thermodynamic properties and the classification of solutions. *Ind. & Eng. Chem.* **40**, 345–348 (1948).

49. Hillert, M. & Jarl, M. A model for alloying in ferromagnetic metals. *Calphad* **2**, 227–238 (1978).

50. Inden, G. Project meeting calphad v. *Ch.* **111** **4**, 1–13 (1976).

51. Andersson, J.-O., Helander, T., Höglund, L., Shi, P. & Sundman, B. Thermo-calc & dictra, computational tools for materials science. *Calphad* **26**, 273–312 (2002).

52. Yang, Y. et al. A diffuse-interface model of anisotropic interface thermal conductivity and its application in thermal homogenization of composites. *Scr. Mater.* **212**, 114537 (2022).

53. Moelans, N., Blanpain, B. & Wollants, P. Quantitative analysis of grain boundary properties in a generalized phase field model for grain growth in anisotropic systems. *Phys. Rev. B* **78**, 024113 (2008).

54. Turnbull, D. Theory of grain boundary migration rates. *JOM* **3**, 661–665 (1951).

55. Gusarov, A. V., Yadroitsev, I., Bertrand, P. & Smurov, I. Model of radiation and heat transfer in laser-powder interaction zone at selective laser melting. *ASME. J. Heat Transf.* **131**, 072101 (2009).

56. Nicoli, M., Plapp, M. & Henry, H. Tensorial mobilities for accurate solution of transport problems in models with diffuse interfaces. *Phys. Rev. E* **84**, 046707 (2011).

57. Sih, S. S. & Barlow, J. W. The prediction of the emissivity and thermal conductivity of powder beds. *Part. Sci. Technol.* **22**, 427–440 (2004).

58. Denlinger, E. R., Jagdale, V., Srinivasan, G., El-Wardany, T. & Michaleris, P. Thermal modeling of inconel 718 processed with powder bed fusion and experimental validation using in situ measurements. *Addit. Manuf.* **11**, 7–15 (2016).

59. Voigt, W. Ueber die beziehung zwischen den beiden elastizitätsconstanten isotroper körper. *Annalen der physik* **274**, 573–587 (1889).

60. Schneider, D. et al. Phase-field elasticity model based on mechanical jump conditions. *Comput. Mech.* **55**, 887–901 (2015).

61. Durga, A., Wollants, P. & Moelans, N. A quantitative phase-field model for two-phase elastically inhomogeneous systems. *Comput. Mater. Sci.* **99**, 81–95 (2015).

62. Dunne, F. & Petrinic, N. *Introduction to Computational Plasticity* (Oxford University Press on Demand, 2005).

63. Simo, J. C. & Hughes, T. J. *Computational inelasticity*, vol. 7 (Springer Science & Business Media, 2006).

64. Aagesen, L. K., Schwen, D., Ahmed, K. & Tonks, M. R. Quantifying elastic energy effects on interfacial energy in the kim-kim-suzuki phase-field model with different interpolation schemes. *Comput. Mater. Sci.* **140**, 10–21 (2017).

65. Chatterjee, S., Schwen, D. & Moelans, N. An efficient and quantitative phase-field model for elastically heterogeneous two-phase solids based on a partial rank-one homogenization scheme. *Int. J. Solids Struct.* **250**, 111709 (2022).

66. Kim, S. G., Kim, W. T. & Suzuki, T. Phase-field model for binary alloys. *Phys. Rev. E* **60**, 7186 (1999).

67. Vaithyanathan, V. & Chen, L. Coarsening of ordered intermetallic precipitates with coherency stress. *Acta Mater.* **50**, 4061–4073 (2002).

68. Hillert, M. *Phase equilibria, phase diagrams and phase transformations: their thermodynamic basis* (Cambridge University Press, 2007).

69. Hillert, M. Solute drag, solute trapping and diffusional dissipation of gibbs energy. *Acta Mater.* **47**, 4481–4505 (1999).

70. Wang, H., Zhang, X., Lai, C., Kuang, W. & Liu, F. Thermodynamic principles for phase-field modeling of alloy solidification. *Curr. Opin. Chem. Eng.* **7**, 6–15 (2015).

71. Steinbach, I., Zhang, L. & Plapp, M. Phase-field model with finite interface dissipation. *Acta Mater.* **60**, 2689–2701 (2012).

72. Andersson, J.-O. & Ågren, J. Models for numerical treatment of multicomponent diffusion in simple phases. *J. Appl. Phys.* **72**, 1350–1355 (1992).

73. Ardell, A. J. Gradient energy, interfacial energy and interface width. *Scr. Mater.* **66**, 423 (2012).

74. Jönsson, B. Assessment of the mobilities of cr, fe, and ni in fcc cr-fe-ni alloys. *Int. J. Mater. Res.* **86**, 686–692 (1995).

75. Bonin, R., Schneider, M., Silva, T. J. & Nibarger, J. P. Dependence of magnetization dynamics on magnetostriction in nife alloys. *J. Appl. Phys.* **98**, 123904 (2005).

76. Coey, J. M. *Magnetism and magnetic materials* (Cambridge University Press, 2010).

77. Exl, L. et al. Labonte's method revisited: an effective steepest descent method for micromagnetic energy minimization. *J. Appl. Phys.* **115**, 17D118 (2014).

78. Schabes, M. E. & Bertram, H. N. Magnetization processes in ferromagnetic cubes. *J. Appl. Phys.* **64**, 1347–1357 (1988).

79. Furuya, A. et al. Semi-implicit steepest descent method for energy minimization and its application to micromagnetic simulation of permanent magnets. *IEEE Trans. Magn.* **51**, 1–4 (2015).

80. Fangohr, H. et al. A new approach to (quasi) periodic boundary conditions in micromagnetics: The macrogeometry. *J. Appl. Phys.* **105**, 07D529 (2009).

81. Fritsch, D. & Ederer, C. First-principles calculation of magnetoelastic coefficients and magnetostriction in the spinel ferrites cofe2o4 and nife2o4. *Phys. Rev. B* **86**, 014406 (2012).

82. Tonks, M. R., Gaston, D., Millett, P. C., Andrs, D. & Talbot, P. An object-oriented finite element framework for multiphysics phase field simulations. *Comput. Mater. Sci.* **51**, 20–29 (2012).

83. Permann, C. J. et al. Moose: Enabling massively parallel multiphysics simulation. *SoftwareX* **11**, 100430 (2020).

84. Otis, R. & Liu, Z.-K. Pycalphad: CALPHAD-based Computational Thermodynamics in Python. *J. Open Res. Softw.* **5**, 1 (2017).

85. Šmilauer, V. et al. Yade Documentation 3rd ed. The Yade Project. https://doi.org/10.5281/zenodo.5705394 (2021).

86. Balay, S. et al. PETSc Users Manual. Argonne National Laboratory. https://ora.ox.ac.uk/objects/uuid:fa2b9e7c-1c58-429c-90fd-f780a3c3dc7d (2019).

ACKNOWLEDGEMENTS

AUTHOR CONTRIBUTIONS

Conceptualization: B.-X.X. and Y.Y.; methodology: Y.Y. and B.-X.X.; software: Y.Y. and X.Z.; validation: T.D.O. and Y.Y.; investigation: Y.Y. and T.D.O.; formal analysis: Y.Y. and T.D.O.; resources, Y.Y. and K.A.; data curation, Y.Y.; writing—original draft preparation, Y.Y. and T.D.O.; writing—review and editing, Y.Y., T.D.O., X.Z., K.A. and B.-X.X.; visualization, Y.Y.; supervision, B.-X.X.; consultation and discussion, K.A.; funding acquisition, B.-X.X. All authors have read and agreed to the published version of the manuscript.

FUNDING

COMPETING INTERESTS

The authors declare no competing interests.

ADDITIONAL INFORMATION

Supplementary information The online version contains supplementary material available at https://doi.org/10.1038/s41524-023-01058-9.

Correspondence and requests for materials should be addressed to Yangyiwei Yang or Bai-Xiang Xu.

Reprints and permission information is available at http://www.nature.com/reprints

Publisher's note Springer Nature remains neutral with regard to jurisdictional claims in published maps and institutional affiliations.